The survey of planetary nebulae in Andromeda (M31). IV. Radial oxygen and argon abundance gradients of the thin and thicker disc

Souradeep Bhattacharya,[1★] Magda Arnaboldi,[2] Nelson Caldwell,[3] Ortwin Gerhard,[4] Chiaki Kobayashi[5] Johanna Hartke,[6] Kenneth C. Freeman,[7] Alan W. McConnachie,[8] and Puragra Guhathakurta[9]

[1]*Inter University Centre for Astronomy and Astrophysics, Ganeshkhind, Post Bag 4, Pune 411007, India*
[2]*European Southern Observatory, Karl-Schwarzschild-Str. 2, 85748 Garching, Germany*
[3]*Harvard-Smithsonian Center for Astrophysics, 60 Garden Street, Cambridge, MA 02138, USA*
[4]*Max-Planck-Institut für extraterrestrische Physik, Giessenbachstraße, 85748 Garching, Germany*
[5]*Centre for Astrophysics Research, Department of Physics, Astronomy and Mathematics, University of Hertfordshire, Hatfield, AL10 9AB, UK*
[6]*European Southern Observatory, Alonso de Córdova 3107, Santiago de Chile, Chile*
[7]*Research School of Astronomy and Astrophysics, Mount Stromlo Observatory, Cotter Road, ACT 2611 Weston Creek, Australia*
[8]*NRC Herzberg, 5071 West Saanich Road, Victoria, BC V9E 2E7, Canada*
[9]*UCO/Lick Observatory, Department of Astronomy & Astrophysics, University of California Santa Cruz, 1156 High Street, Santa Cruz, California 95064, USA*

arXiv:2203.06428v2 [astro-ph.GA] 20 Sep 2022

Accepted September 16, 2022. Received September 16, 2022; in original form February 21, 2022

ABSTRACT

We obtain a magnitude-limited sample of Andromeda (M 31) disc PNe with chemical abundance estimated through the direct detection of the [O III] 4363 Å line. This leads to 205 and 200 PNe with oxygen and argon abundances respectively. We find that high- and low-extinction M 31 disc PNe have statistically distinct argon and oxygen abundance distributions. In the radial range 2 – 30 kpc, the older low-extinction disc PNe are metal-poorer on average with a slightly positive radial oxygen abundance gradient (0.006 ± 0.003 dex/kpc) and slightly negative for argon (−0.005 ± 0.003 dex/kpc), while the younger high-extinction disc PNe are metal-richer on average with steeper radial abundance gradients for both oxygen (−0.013 ± 0.006 dex/kpc) and argon (−0.018 ± 0.006 dex/kpc), similar to the gradients computed for the M 31 HII regions. The M 31 disc abundance gradients are consistent with values computed from major merger simulations, with the majority of the low-extinction PNe being the older pre-merger disc stars in the thicker disc, and the majority of the high-extinction PNe being younger stars in the thin disc, formed during and after the merger event. The chemical abundance of the M 31 thicker disc has been radially homogenized because of the major merger. Accounting for disc scale-lengths, the positive radial oxygen abundance gradient of the M 31 thicker disc is in sharp contrast to the negative one of the MW thick disc. However, the thin discs of the MW and M 31 have remarkably similar negative oxygen abundance gradients.

Key words: Galaxies: individual (M 31) – Galaxies: evolution – Galaxies: structure – planetary nebulae: general

1 INTRODUCTION

Late-type galaxies can contain multi-layered populations that are kinematically distinct, the "cold" thin disc and the "hot" thick disc, found in the Milky Way (MW; e.g. Gilmore & Reid 1983) and in nearby galaxies (Yoachim & Dalcanton 2006; Comerón et al. 2019). The MW thick disc within the solar radius is found to be chemically distinct from the MW thin disc suggesting separate evolution for the two (e.g. Bland-Hawthorn & Gerhard 2016; Kobayashi et al. 2020). Thick discs may form from accreted gas during a chaotic period of hierarchical clustering at high redshift (Brook et al. 2004) or from dynamical heating of thinner discs by secular processes (Sellwood 2014). Mergers with satellites can also dynamically heat thin discs to decrease their rotational velocity and increase their velocity dispersion (Quinn & Goodman 1986), resulting in thickened discs (Hopkins et al. 2009). Even the stars from the merged satellite can form the thick disc (Peñarrubia et al. 2006).

Since galaxies are thought to evolve by hierarchical mergers with satellite galaxies (White & Rees 1978; Bullock & Johnston 2005), late-type galaxies of varying disc thickness are expected. Observational evidence of multi-layered disks in nearby spirals can be obtained by measuring kinematics and metallicity of their stellar populations covering a large radial range in these discs (E.g. Yoachim & Dalcanton 2008a,b). However, this requires deep spectroscopic observations of resolved stars (E.g. Guhathakurta et al. 2005) or integral field spectroscopy (E.g. Saglia et al. 2018). For the nearly 12 sq. deg. on-sky coverage of the M 31 disc, such observations would be highly time consuming with current instrumentation.

However, spectroscopic observations for kinematics and chemistry is possible with a reasonable investment in telescope time with discrete tracers, such as Planetary Nebulae (PNe). PNe are discrete tracers of stellar population properties and their kinematics have been measured in galaxies of different morphological types (e.g. Coccato et al. 2009; Cortesi et al. 2013; Pulsoni et al. 2018; Aniyan et al.

★ E-mail: souradeep@iucaa.in

© 2022 The Authors

2018; Hartke et al. 2018; Aniyan et al. 2021; Hartke et al. 2022). In particular, in Bhattacharya et al. (2019b, hereafter Paper II), through velocity dispersion profiles of high- and low- extinction PNe in the M 31 disc, kinematically distinct dynamically colder thin and hotter thicker discs were respectively identified. The thin and thicker discs of M 31 were found to have rotational velocity dispersions twice and thrice that of the MW disc population of the same age (Paper II, Collins et al. 2011; Dorman et al. 2015). While the MW disc is thought to have evolved mainly by secular evolution (Sellwood 2014) with its most recent merger ∼10 Gyr ago (Belokurov et al. 2018; Helmi et al. 2018), the age-velocity dispersion relation in the M 31 disc at galactocentric radial distances R_{GC} =14–20 kpc was found to be consistent with a ∼1:5 major merger in M 31 ∼2.5–4.5 Gyr ago. A minor merger, such as that modelled for M 31 by Fardal et al. (2013), would not be able to dynamically heat the M 31 disc to the measured rotational velocity dispersion for the thicker disc (E.g. see models by Martig et al. 2014). Thus, while the MW is a prime laboratory for studying effects driven by secular evolution in discs, the M 31 disc formation is considered to be primarily driven by mergers (Paper II) also supported by observational evidence of substructures in its inner halo (PAndAS – McConnachie et al. 2009).

The measured rotational velocity dispersions for the M 31 thin and thicker disc is in agreement with predictions from the merger simulations by Hammer et al. (2018). There a gas-rich satellite was accreted on to M 31 with an orbit along the Giant Stream, heating the M 31 disc and producing a thick disc from the pre-existing stars. After the merger, the replenished cold gas would lead to the formation of a gaseous thin disc with younger stars formed through a burst of star formation. The stars in the thin and thick discs of M 31 are formed in different epochs in this scenario and so differences may be present in the chemical composition of their stars. See also the N-body simulations of a merger (mass ratio including dark matter ∼1:5) in M 31 by Milošević et al. (2022) as well as the suite of N-body simulations by Sadoun et al. (2014).

The chemical evolution of discs of spiral galaxies is also reflected in their radial abundance distributions. In an inside-out build-up scenario of a galaxy disc, negative radial metallicity gradients are expected (e.g. Sánchez-Menguiano et al. 2018). Hydrodynamical simulations have shown that the radial metallicity gradient in galaxies is modified both in case of secular evolution (e.g. Gibson et al. 2013) and also in the case of galaxy mergers (e.g. Zinchenko et al. 2015; Tissera et al. 2019).

Abundance distributions in galaxies can be mapped from PNe, as they are tracers of chemistry in galaxies (Maciel & Koppen 1994; Kwitter & Henry 2021). PN elemental abundances, particularly oxygen and argon, shed light on the ISM conditions at the time of formation of their parent stellar population (e.g. Bresolin et al. 2010; Hernández-Martínez et al. 2011; Stanghellini et al. 2014). When PNe ages can be identified, it becomes possible to map abundance variations across different epochs of star formation in galaxies. In the MW, the radial oxygen abundance gradient for both thin and thick disc PNe formed at different epochs have been obtained separately allowing for significant constraints on its chemical evolution (Stanghellini & Haywood 2018).

In the case of M 31, the PN oxygen abundance gradient has previously been computed by Sanders et al. (2012) from ∼ 50 observed PNe in the M 31 disc. They found a best-fit slope of −0.0056±0.0076 dex/kpc within R_{GC} ∼4–24 kpc. Later estimates by Kwitter et al. (2012) (only oxygen abundances) and Peña & Flores-Durán (2019) (both oxygen and argon abundances) out to R_{GC} ∼ 110 kpc have also found near-flat abundance gradients. The flat PN oxygen abundance gradient differs from that derived for HII regions in the M 31 disc which display a much steeper best-fit slope of −0.023 ± 0.002 dex/kpc (Zurita & Bresolin 2012). Since HII regions sample only a young (<0.3 Gyr) stellar population, while PNe sample a wider age range, the difference in abundance gradients of the two samples may reflect the different properties of their parent generations of stars. Elemental abundances of the high- and low- extinction PNe with distinct ages can now be computed to obtain separate abundance distributions of the kinematically distinct thin and thicker disc in M 31 (Paper II).

In this paper we obtain direct estimates of oxygen and argon abundances for the M 31 disc PNe using a large sample size and covering a wide 2 − 30 kpc radial range. Our aim is to assess whether the kinematically distinct thin and thicker disc of M 31 have different abundance distribution and gradients. Our observations and sample selection are discussed in Section 2. The radial oxygen and argon abundance gradients of the high- and low-extinction PNe respectively, are presented in Section 3. We note that the radial gradient of the log(O/Ar) ratios and the distribution of PNe in the log(O/Ar) vs. 12+ log(Ar/H) planes are shown and presented in Arnaboldi et al. (2022, companion paper, hereafter Paper V). We assess our radial abundance gradients in context of disc galaxies in Section 4. We then discuss constraints on the chemical evolution and formation history of M 31 in Section 5 and finally conclude in Section 6.

2 DATA REDUCTION AND SAMPLE SELECTION

2.1 Observations

In Bhattacharya et al. (2019a, hereafter Paper I), we identified PN candidates in a 16 sq. deg. imaging survey of M 31 with MegaCam at the CFHT, covering the disc and inner halo. This was later expanded to cover 54 sq. deg in M31 (Bhattacharya et al. 2021, hereafter Paper III). Spectroscopic observations of a complete subsample of these PN candidates were carried out with the Hectospec multifibre positioner and spectrograph on the Multiple Mirror Telescope (MMT; Fabricant et al. 2005). The Hectospec 270 gpm grating was used and provided spectral coverage from 3650 to 9200 Å at a resolution of ∼ 5 Å. Some spectra did not cover [O II] 3726/3729 Å because of the design of the spectrograph (alternate fibers are shifted by 30 Å) and the small blueshift of M 31. Each Hectospec fibre subtends 1.5″ on the sky and was positioned on the PN candidates in each field. Table 1 shows details of the fields observed in this work whose positions have been marked in Figure 1. We targeted 2222 distinct PNe candidates with fibres in 26 separate fields in M 31, some of which were observed multiple times. Of these fields, seven were part of tag-along observations (where only a few free fibres from other observing programs covering M31 were placed on the PN candidates). These pointings are marked with * in Table 1.

The initial steps for the data reduction of each Hectospec spectra are similar to that described by Caldwell et al. (2009) for their observations of star clusters in M 31, which were also followed by Sanders et al. (2012) for their PN spectra. Briefly, following the debiasing and flat-fielding of each observed field, individual spectra were extracted and wavelength calibrated, including a heliocentric correction. Standard star spectra were used for flux calibration and instrumental response. Sky subtraction was carried out by averaging spectra from fibers placed on blank sky from the same exposures or by offsetting the telescope by a few arcseconds (see Caldwell et al. 2009). The spectra of PN candidates that were observed multiple times (in adjacent fields) have been combined, effectively coadding those integration times. Figure 2 shows an example of the observed PN spectra.

Table 1. Details of MMT Hectospec observations of PNe. Brighter PNe were prioritised for observations but PNe to m_{5007} = 26.4 mag were targeted. Some PNe were observed twice in the regions of overlap of adjacent fields. The fields for tag-along observations are marked with *.

Obs. date	RA (deg)	DEC (deg)	Exp. time (s)	$N_{PN,targ}$	$N_{PN,obs}$
14.09.18*	10.4700833	41.0778389	9000	38	19
15.09.18	11.2468750	39.3372003	4800	41	13
06.10.18*	10.4700833	41.0778389	9000	65	41
04.12.18	11.5407083	42.7038650	3600	202	44
02.09.19	10.83	40.645	4800	148	67
05.09.19	10.0681250	39.9762458	3600	119	55
23.10.19	9.4446667	40.4633331	4800	175	71
24.10.19	10.8910833	41.5916672	4800	226	174
25.10.19	9.0818750	39.6116675	6000	79	26
07.10.20*	10.659625	41.1844253	7920	44	22
07.10.20*	10.15525	40.9850014	6600	53	21
08.10.20*	10.8875833	41.4929542	8400	37	26
08.10.20	11.568125	41.4599992	4800	232	63
09.10.20*	10.15525	40.9850014	5280	88	34
09.10.20*	11.2415417	41.8282319	7560	30	18
10.10.20*	10.2915417	40.7175942	3000	45	17
10.10.20	9.7178333	41.5566672	4800	110	28
11.10.20*	11.2415417	41.8282319	7560	8	3
12.10.20*	11.4205	42.0603333	4500	26	14
12.10.20*	11.4205	42.0603333	6000	27	16
12.10.20	12.2790417	42.4166681	4800	166	26
12.10.20	10.5755	42.3983344	6000	153	37
13.10.20	8.5034167	40.7700006	4800	26	8
13.10.20	12.44075	43.9933319	4800	13	5
24.10.20	10.6455667	41.2599983	3000	228	57
24.10.20	11.8477083	38.5099983	5760	30	16
24.10.20*	10.2915417	40.7175942	4800	135	58
25.10.20	13.06125	42.3266678	6000	80	17
25.10.20	12.7429167	40.9850006	3600	42	8
25.10.20	8.919125	41.9350014	3600	23	5
25.10.20	9.8354167	43.3883325	6000	69	12

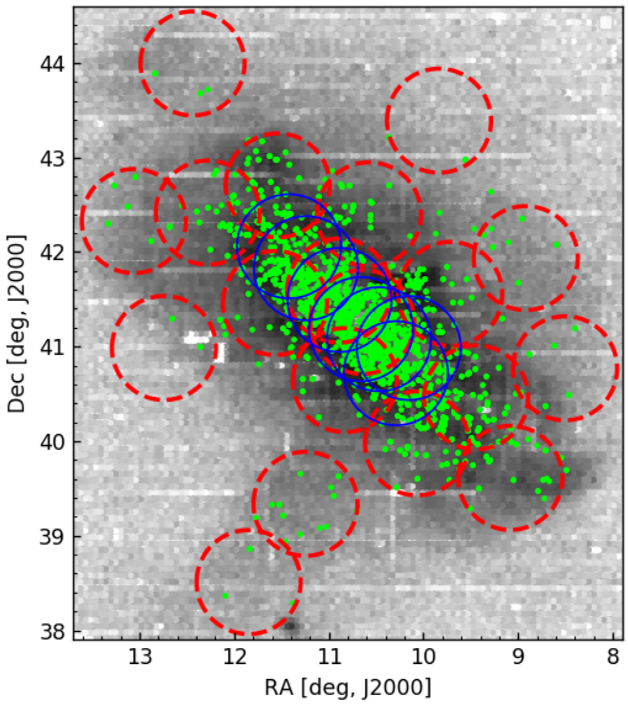

Figure 1. Position on sky of the PNe with V_{LOS} measurements in M31, both observed in this work as well as the archival sample from Sanders et al. (2012), overlaid on the PAndAS number density map of RGB stars(McConnachie et al. 2018). The targeted MMT fields are marked in red while those utilised in tag-along observations are marked in blue.

2.2 Emission line fluxes and line-of-sight velocity estimation

Emission-line fluxes for each PN candidate were measured using the automated line fitting algorithm, ALFA (Wesson 2016), which has been tailored for emission line sources. The line-of-sight velocity (V_{LOS}) is measured from the strongest emission-lines accounting for heliocentric correction, with an uncertainty of 3 km s^{-1}. After subtracting a globally-fitted continuum, ALFA derives fluxes by optimising the parameters of Gaussian fits to line profiles using a genetic algorithm. Of the 2222 targeted PNe candidates, 866 have confirmed detection of the [O III] 4959/5007 Å emission lines. The [O III] 5007 Å emission line is detected in all these cases with a signal-to-noise ratio higher than 5. All of them have Hα emission line present also. The fraction of PNe detected as a function of magnitude is shown in Figure 3. We also used ALFA to obtain the emission line fluxes from the archival Hectospec spectra of 449 PNe studied by Sanders et al. (2012) which had confirmed detection of the [O III] 4959/5007 Å emission lines. Of these archival PNe, 64 were re-observed in this work. We thus have 1251 unique PNe with V_{LOS} measurements in M31, termed the *PN_M31_LOSV* sample. Their spatial position is shown in Figure 1. Note that contaminant spatially unresolved HII regions were removed and are not included in this sample (see Appendix A for further details).

2.3 Extinction measurement

For each PN, the measured emission-line fluxes are then passed to NEAT (Nebular Empirical Analysis Tool; Wesson et al. 2012), which applies an empirical scheme to calculate the extinction and elemental abundances. NEAT calculated the intrinsic c(Hβ) using the flux-weighted ratios of Hα/Hβ, Hγ/Hβ and Hδ/Hβ (whichever pairs are observed) and the extinction law of Cardelli et al. (1989), first assuming a nebular temperature of 10000K and an electron density of 1000 cm^{-3}, and then recalculating c(Hβ) at the computed temperature and density (whenever available; see Section 2.5 for details). Of the 1251 PNe in the *PN_M31_LOSV* sample, 745 had the Hβ line detected and their extinctions (A_V) could be determined with a positive value. Note that a further 380 PNe showed the presence of the Hβ line but resulted in a negative (but close to zero) value of A_V, similar to what was found by Sanders et al. (2012). These PNe were not utilised further in this work to derive elemental abundances but are a part of the *PN_M31_LOSV* sample.

2.4 Selection of M 31 disc PNe from the position velocity diagram

The PNe with extinction measurements are de-projected on to the galaxy plane based on the position angle (PA = 38°) and inclination (i = 77°) of M 31 in the planar disc approximation. PNe beyond R_{GC} = 30 kpc are not included further in the analysis, as a significant fraction of them may be associated with the prominent bright substructures – G1-Clump and Northern Spur, and the dwarf galaxy NGC 205, present at these radii. The remaining PNe within R_{GC} = 30 kpc are shown in Figure 4 which plots their position, X_{GC} (de-projected major-axis distance in deg in the disc-plane), against their $V_{LOSV} - V_{sys}$ (M 31 systemic velocity, V_{sys} = −309 km

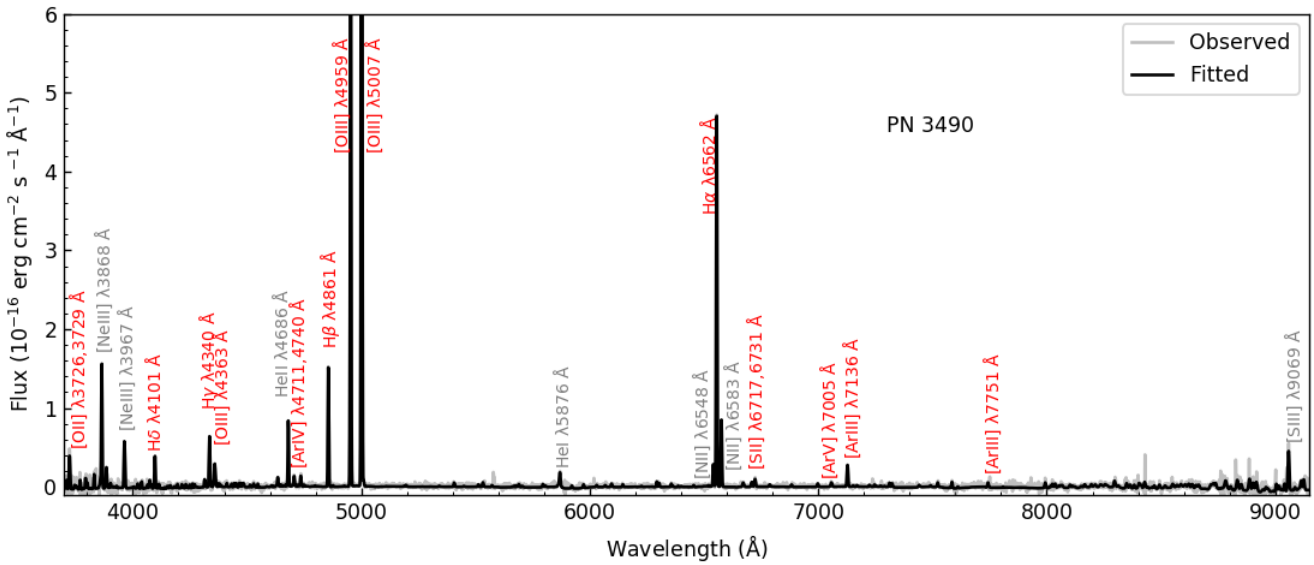

Figure 2. An example of the spectra observed by Hectospec for the PNe in M31. The spectra shown in grey is obtained following heliocentric correction, removal of sky-lines and flux calibration. The fitted spectra from ALFA (Wesson 2016) is shown in black. The emission lines with fluxes tabulated in Table B1 are labelled in red, while other observed bright lines are marked in grey.

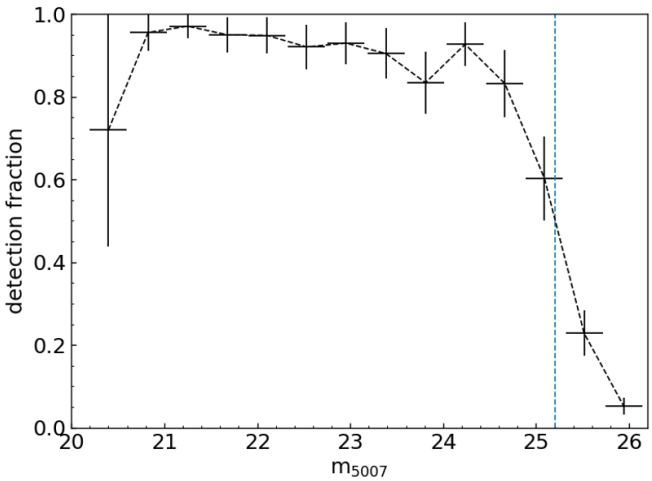

Figure 3. Fraction of PNe targeted with spectroscopic observations where [O III] 4959/5007 Å emission lines (the [O III] doublet) is detected. The uncertainty in detection fraction is the binomial proportion confidence-interval of observed PNe in any magnitude bin obtained using the Wilson score interval method (Wilson 1927). The blue dashed line shows the 50% detection limit of the spectroscopic follow-up.

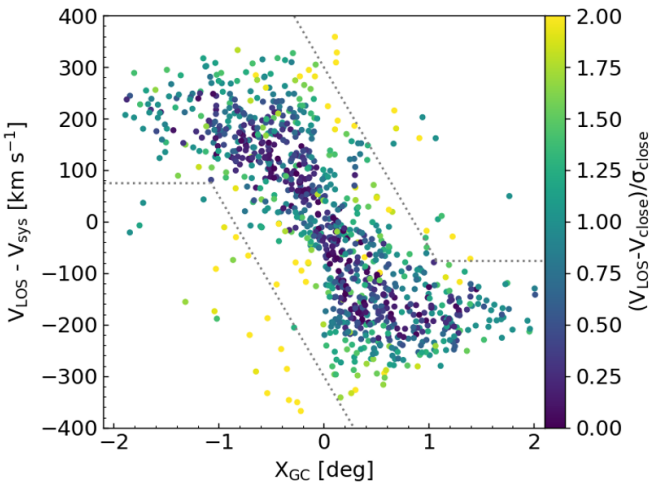

Figure 4. Position-velocity diagram of PNe within R_{GC} = 30 kpc. Here X_{GC} is the deprojected major-axis distance in deg (1 deg= 13.68 kpc). The dotted lines distinguish the outliers which have a non-disc angular momentum and possibly correspond to streams or halo PNe. The PNe are coloured by their $(V_{LOS} - V_{close})/\sigma_{close}$ values, where the outliers stand out in yellow. V_{close} and σ_{close} refer to the local LOSV and dispersion within a radius of 4′ centred around each PN.

s^{-1}; Merrett et al. 2006). While the majority of PNe in M 31 within R_{GC} = 30 kpc are associated with its bulge and disc, some PNe associated with the extension of a luminous substructure or any fainter stellar stream co-spatial with the disc may also be present. Such PNe may present themselves as a dynamically cold component that is offset from the main disc PNe distribution in the position-velocity plot, like the PNe associated with the extension of the Giant Stream on the disc as proposed by Merrett et al. (2003). The dotted lines in Figure 4 correspond to an offset from the mean value of the $V_{LOSV} - V_{sys}$ for the PNe to the maximum possible velocity dispersion of the thick disc in M 31 (160 km s^{-1}; from Paper II). We identify the position-velocity outliers as those PNe whose $V_{LOSV} - V_{sys}$ values are outside the maximum values for the thick disc PNe in M 31. This selection successfully identifies as outliers those PNe on the extension of the giant stream tagged previously by Merrett et al. (2003) and a few additional PNe.

A further selection of PN outliers is possible for the inner regions of the disc with large number of PN LOSV measurements, where such LOSV outliers may stand out from the LOSVs of the PNe in their

Table 2. Summary of numbers of PNe observed in this work and Sanders et al. (2012) to build the total sample of M 31 disc PNe with LOSV and A_V measurements.

No. of PNe with LOSV measurement observed in this work	866
No. of Sanders et al. (2012) PNe with LOSV measurement	449
Total PNe with LOSV measurement (*PN_M31_LOSV*)	1251
Those of the above with positive A_V measurement	745
Those of the above in the disc (*PN_M31d_Av*)	601

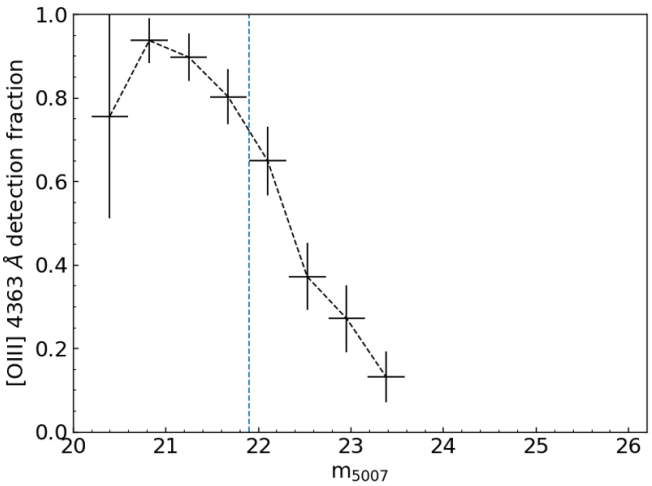

Figure 5. Fraction of PNe with spectroscopic observations where the [O III] 4363 Å emission line is detected and the elemental abundances could be derived. The uncertainty in detection fraction is the binomial proportion confidence-interval of observed PNe in any magnitude bin obtained using the Wilson score interval method (Wilson 1927). The blue dashed line shows the 75% detection limit of the [O III] 4363 Å emission line.

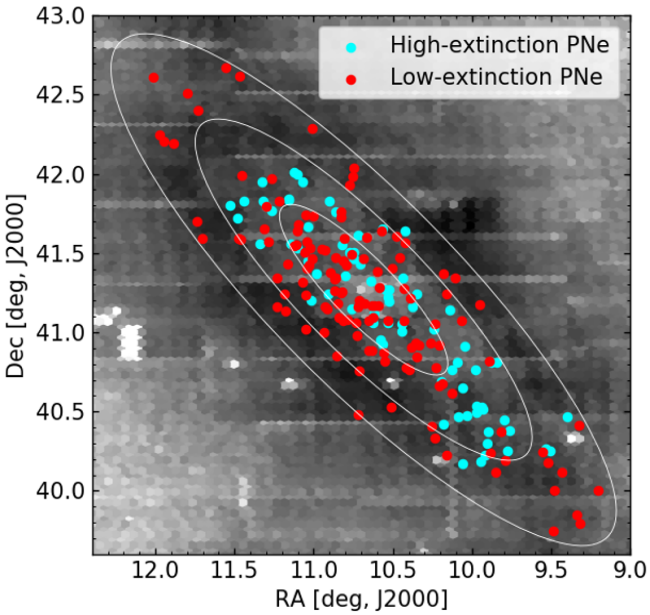

Figure 6. Position on sky of the PNe with oxygen abundances determined in M31, overlaid on the PAndAS number density map of RGB stars(McConnachie et al. 2018). The high- and low-extinction PNe are marked in cyan and red respectively. The white ellipses show R_{GC} = 10, 20, 30 kpc respectively.

local spatial neighbourhood. For each PN, we obtain the mean local LOSV, V_{close}, and local LOSV dispersion,σ_{close}, within a radius of 4′. The value of the radius was chosen such that there are at least 5 PNe within such radius for each PNe out to $R_{GC} \sim 20$. Those PNe whose LOSV is over $2\sigma_{close}$ away from V_{close}, are tagged as outliers. In this way, we identify as outliers those PNe associated with the claimed extension of the giant stream from Merrett et al. 2003 as seen in Figure 4, along with additional PNe that were not classified as such in previous works. We thus identify 601 PNe with extinction measurements (see Section 2.3) within R_{GC} = 30 kpc which are robust M 31 disc members (some of these within R_{GC} = 5 kpc may also belong to the M 31 bulge). This is then the M 31 disc PN sample (termed *PN_M31d_Av*) and Table 2 summarises the number of PNe identified in each aforementioned step. This is the largest sample of PNe with extinction measurements observed in the M 31 disc, in fact, in any external galaxy. We have nearly doubled the sample size of PNe with extinction measurements from Paper II. PN disc kinematics with the increased sample will be explored in a future paper. In this work, we further focus on the M 31 disc PN sample in order to study PN elemental abundances.

2.5 Direct determination of elemental abundances for each PN

Emission lines in the spectra of each PN of the *PN_M31d_Av* sample are de-reddened using the calculated c(Hβ) and their temperatures and densities are calculated using an iterative process from the relevant diagnostic lines using NEAT (see Wesson et al. 2012, section 3.3). For our observations, NEAT utilizes the temperature-sensitive [O III] 4363 Å line[1] and the density-sensitive [O II] 3726/3729 Å and [S II] 6717/6731 Å doublets to obtain temperature and electron density for each PN, whenever the [O III] 4363 Å line[2] is observed. Oxygen and argon ionic abundances are derived from the observed fluxes of the oxygen ([O II] 3726/3729 Å, [O III] 4363/4959/5007 Å) and argon ([Ar III] 7136/7751 Å, [Ar IV] 4711/4740 Å, [Ar V] 7005 Å) emission lines respectively. Elemental oxygen and argon abundances are obtained from the ionic abundances using the ionisation correction factors (ICFs) from Delgado-Inglada et al. (2014) where applicable following the default NEAT prescription (see Appendix B3 for details). Uncertainties are propagated through all steps of the analysis into the final values. Comparison with archival PN abundance determinations is discussed in Appendix B4. Of the 601 PNe in the *PN_M31d_Av* sample, 276 have oxygen abundances determined, out of which 269 also have argon abundances.

Figure 5 shows the detection fraction of the temperature-sensitive [O III] 4363 Å emission line, enabling the computation of oxygen and argon abundances, for those PNe with spectroscopic observations. The [O III] 4363 Å emission line, relative to the [O III] doublet, is brighter for lower metallicity PNe. Hence, we are more likely to detect the [O III] 4363 Å emission line in metal-poor PNe

[1] Note that the temperature sensitive [N II] 5755 Å line is also observed for some PNe in our sample. However, the derived [N II]-based temperature is more uncertain than the [O III]-based temperature while also being inherently less reliable (see Appendix B2). Thus only the [O III]-based temperature is used for chemical abundance computation in this work.

[2] We ignore recombination contribution to the [O III] 4363 Å line as the relevant recombination lines are much too faint to be observed at the distance of M 31 with present day instrumentation/telescopes.

Table 3. Properties of the 205 M 31 PNe in the *PN_M31d_O_lim* sample. Column 1: Serial number of the PN in this work. Following IAU naming conventions, each PN should be designated as SPNA<Sl. No.>. E.g. PN 419 should be termed SPNA419; Column 2–3: spatial position of the PN; Column 4: LOSV of the PN; Column 5: Measured balmer decrement of the PN and corresponding extinction in Column 6; Column 7–8: Derived abundances of the PN; Column 9: The [O III] 5007 Å magnitude measured in Paper I and Paper III. A portion of this table is shown here for guidance; the full table will be made available through the CDS.

Sl. No.	RA [J2000] deg	DEC [J2000] deg	V_{LOS} km s^{-1}	c(Hβ) mag	A_V mag	T_e K	N_e cm^{-3}	12+log(O/H)	12+log(Ar/H)	m_{5007} mag
478	11.3247088	41.9470492	-223.5	0.68	1.44	12100^{+400}_{-400}	418^{+945}_{-417}	8.52 ± 0.04	6.28 ± 0.07	21.2
496	11.2640144	41.9713806	-125.7	0.32	0.69	11800^{+400}_{-400}	2450^{+955}_{-1360}	8.68 ± 0.1	6.39 ± 0.05	21.03
942	12.0147552	42.610521	-102.0	0.18	0.37	11300^{+500}_{-500}	1000	8.35 ± 0.05	6.02 ± 0.04	21.2
945	11.4699967	42.6147482	-174.0	0.09	0.18	10600^{+300}_{-300}	2040^{+1030}_{-590}	8.52 ± 0.04	6.15 ± 0.03	20.82
959	11.5577759	42.6747226	-83.8	0.24	0.51	10100^{+300}_{-300}	2560^{+1450}_{-800}	8.7 ± 0.2	6.16 ± 0.04	21.02

Table 4. Summary of PN selection to build the *PN_M31d_O_lim* sample used in this work from the *PN_M31d_Av* sample. We also summarise the extinction classification of the *PN_M31d_O_lim* sample discussed in Section 2.6.

M 31 disc PN with oxygen abundance	276
M 31 disc PN with argon abundance	269
Magnitude-limited sample with oxygen abundance (*PN_M31d_O_lim*)	205
Those of the previous with argon abundance	200
High-extinction PNe in the *PN_M31d_O_lim*	75
Those of the previous with argon abundance	75
Low-extinction PNe in the *PN_M31d_O_lim*	130
Those of the previous with argon abundance	125

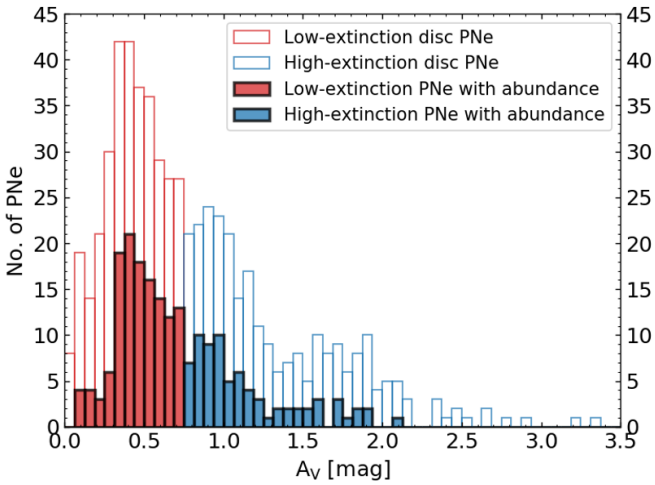

Figure 7. Histogram (shaded) showing the distribution of extinction values of the PNe in the *PN_M31d_O_lim* sample (magnitude limited sample with oxygen abundances determined). The high- and low-extinction PNe lie in the blue and red shaded regions respectively. The histogram (unshaded) shows the distribution of extinction values of the *PN_M31d_Av* sample for comparison.

at the faint end. We thus restrict the analysis of the abundance distribution and gradient to those PNe where the detection fraction is higher than 75%, i.e, $m_{5007} \leq 21.9$mag, so as not to be biased towards metal-poor PNe while still maintaining a large sample, 205 and 200 PNe with oxygen and argon abundance values determined respectively. The magnitude-limited sample of 205 M 31 disc PNe with oxygen abundances is termed the *PN_M31d_O_lim* sample. It is the sample for which the analysis is carried out in this work. Their spatial position is shown in Figure 6. The emission line fluxes of the lines of interest for these PNe have been listed, along with their 1σ uncertainties, in Table B1. Their measured V_{LOS}, A_V, oxygen and argon abundances are listed in Table 3 as well as their observed m_{5007} magnitudes obtained in Paper I and Paper III. In Appendix B4 we compare our independently determined oxygen abundance values with those in the literature for previously observed individual M31 PN spectra. Table 4 summarises the selection of the magnitude-limited abundance sample of M 31 disc PNe from the *PN_M31d_Av* sample. This is the largest sample of PNe with chemical abundances derived in M 31, and in fact, in any external galaxy.

2.6 Classification of planetary nebulae based on extinction measurements

The mass of PN central stars correlates with their circumstellar extinction (Ciardullo & Jacoby 1999). This is because dust production of stars in the AGB phase scales exponentially with their initial progenitor masses for the 1 $\sim$ 2.5$M_\odot$ range after which it remains roughly constant (Ventura et al. 2014). Additionally, PNe with dusty high-mass progenitors evolve faster (Miller Bertolami 2016) and so their circumstellar matter has little time to disperse, while PNe with lower central star masses evolve sufficiently slowly that a larger fraction of dust is dissipated from their envelopes (Ciardullo & Jacoby 1999). In Paper II, the high- and low-extinction PNe constituted the kinematically distinct thin and thicker disc of M 31 respectively. From archival CLOUDY photoionization models (Ferland et al. 1998) of a subsample of these PNe (Kwitter et al. 2012), we found ages of $\sim$ 2.5 and $\sim$ 4.5 Gyr for the high- and low-extinction PNe respectively. As in Paper II, based on the distribution of the M31 PNe extinction values which exhibits a drop at A_V = 0.75 mag, we classify PNe with extinction values higher and lower than A_V = 0.75 mag as high- and low-extinction PNe respectively (for further details, see Section 3.1 in Paper II). Our *PN_M31d_O_lim* sample is then divided into 75 high- and 130 low-extinction PNe, which are expected to be associated with the thin and thicker disc stellar populations respectively, and with age ranges, 2.5 Gyrs and younger (high-extinction PNe), and 4.5 Gyrs and older (low-extinction PNe). All the PNe have oxygen abundances and all but five low-extinction PNe also have argon abundances. Table 4 also summarises the number of high- and low-extinction PNe in the *PN_M31d_O_lim* sample. Figure 7 shows the distribution of extinction values of the PNe in the *PN_M31d_O_lim* sample, along with that for the the M 31 disc PNe sample. The high- and low-extinction PNe are marked separately in Figure 6. As shown in Figure 6 and further discussed in Section 3, the high-extinction

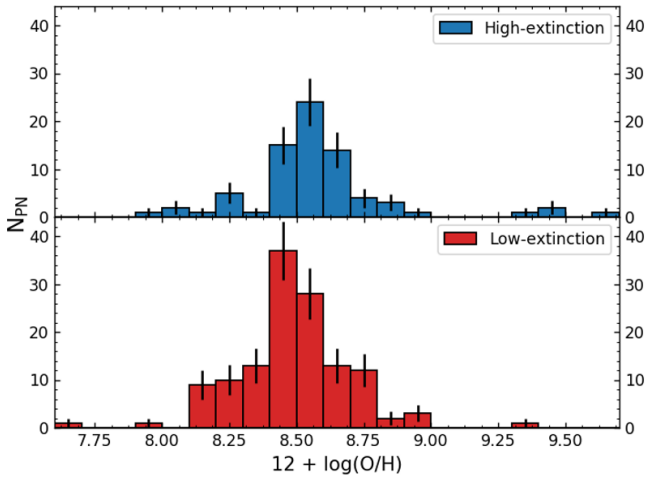

Figure 8. Histogram showing the distribution of oxygen abundances for the [top] high- and [bottom] low-extinction PNe in the *PN_M31d_O_lim* sample. The bins are 0.1 dex wide, vertical bars indicate the Poissonian errors.

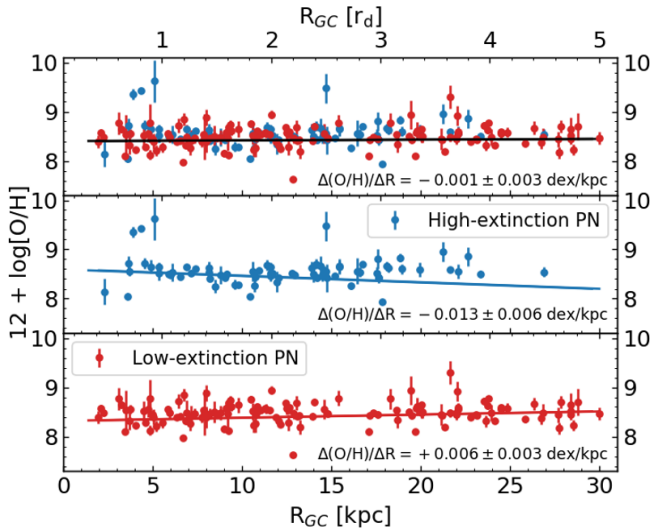

Figure 9. The galactocentric radial distribution of oxygen abundances for [top] all, [middle] high- and [bottom] low-extinction PNe in M 31 in our *PN_M31d_O_lim* sample. The bottom and top axes show R_{GC} in units of kpc and r_d respectively. High- and low-extinction PNe are shown in blue and red respectively. The best-fitting radial oxygen abundance gradient to the *PN_M31d_O_lim* sample is shown for all (black), high- (blue) and low-extinction (red) PNe.

PNe are concentrated within a smaller radial extent than the low-extinction PNe.

3 ABUNDANCE DISTRIBUTION AND RADIAL GRADIENTS IN THE M 31 DISC FROM PLANETARY NEBULAE

We separately explore the chemical abundance distribution and gradients of both oxygen and argon for the high- and low-extinction PNe which trace the kinematically distinct thin and thicker discs of M 31. We note that Delgado-Inglada et al. (2015) suggested a possible dependency of PN oxygen abundance on metallicity and mass for carbon dust rich (CRD) MW PNe. As per their study, CRD MW PNe may be oxygen enriched by up to 0.3 dex from modification of surface oxygen in the Asymptotic Giant Branch (AGB) phase. However, argon has been found to be invariant during the AGB phase, providing an independent probe to the ISM conditions at the time of birth of the PN parent stellar population. We, however, do not find that oxygen is enriched in CRDs in a larger MW PNe sample from Ventura et al. (2017), detailed in Appendix C. Additionally, for PNe evolving from stars with initial mass $\geq 3M_{\odot}$ (younger than $\sim$ 300 Myr), hot-bottom burning (HBB) may result in an oxygen depletion of up to $\sim$ 0.2 dex. The M 31 high- extinction PNe have average ages $\sim$ 2.5 Gyr with the bulk of them having likely formed in a burst of star formation ~2 Gyr ago (Paper II). This implies that a very small number of PNe with very young massive progenitors (affected by HBB) are expected in our sample[3]. The bulk of the M 31 PNe would thus exhibit oxygen and argon abundances unaffected by AGB evolution. Hence we proceed to use oxygen and argon abundances for high- and low-extinction PNe in M31 as probes of the chemical abundances of the ISM at the time of their birth for the different kinematic components of the M 31 disc.

[3] In Paper V, we studied the log(O/Ar) versus 12+log(Ar/H) PN distribution as function of log(N/Ar). We conclude that the log(O/Ar) values did not show any dependency on log(N/Ar) with the implication that the fraction of massive ($\geq 3M_{\odot}$) young ($\sim$ 300 Myr and younger) PNe in the M31 sample is very small.

3.1 Oxygen abundance distribution and radial gradient from Planetary Nebulae

Figure 8 shows the PN oxygen abundance distribution for all the high- and low-extinction PNe in the *PN_M31d_O_lim* sample of the M 31 disc. The mean value of the oxygen abundance for all the high-extinction PNe, $< 12+(O/H) >_{high-ext} = 8.57 \pm 0.03$, is higher than that for all the low- extinction PNe, $< 12 + (O/H) >_{low-ext} = 8.48 \pm 0.02$. While the high-extinction PN sample has higher oxygen abundance on average than the low-extinction sample, there is a considerable overlap in the distributions which is reflected in the large standard deviation values $\sigma(12 + (O/H))_{high-ext} = 0.28$ and $\sigma(12 + (O/H))_{low-ext} = 0.21$. We can establish whether the oxygen abundance distributions of the two PN samples are different by statistically comparing them. We utilize the two-sample Anderson-Darling test (AD-test; Scholz & Stephens 1987) to compare the two distributions, which yields a significance level of 2.3%. Since the significance level is lower than 5%, the null hypothesis that the two samples are drawn from the same distribution is rejected. The difference in the oxygen abundance distributions of the two PN populations stems from the distinct ISM conditions at the time of their birth.

Figure 9 shows the galactocentric radial distribution of PN oxygen abundances for all PNe, as well as distinctly for high- and low-extinction PNe, in the *PN_M31d_O_lim* sample. We note that the high-extinction PNe cover a smaller radial extent than the low-extinction PNe, i.e. the thicker disc in M 31 is more radially extended than the thin disc (see also Yoachim & Dalcanton 2006 for more examples of thin discs embedded in thicker discs). The best-fit parameters are noted in Table 5. For the *PN_M31d_O_lim* sample, we find a near-flat abundance gradient for all PNe, $(\Delta(O/H)/\Delta R)_{all} = 0.001 \pm 0.003$ dex/kpc, a steeply negative oxygen abundance gradient for the high-extinction PNe, $(\Delta(O/H)/\Delta R)_{high-ext} = -0.013 \pm 0.006$ dex/kpc while for the low-extinction PNe we find a slightly positive oxygen abundance gradient, $(\Delta(O/H)/\Delta R)_{low-ext} = 0.006 \pm 0.003$ dex/kpc. Zurita & Bresolin

Table 5. Fitted parameters for radial gradients in the M 31 disc from the *PN_M31d_O_lim* sample.

PN sample	X	X_0	$\Delta X/\Delta R$ dex/kpc	$\Delta X/\Delta R$ dex/r_d
All	12+log(O/H)	8.4 ± 0.04	0.001 ± 0.003	0.006 ± 0.018
High-extinction	12+log(O/H)	8.6 ± 0.08	-0.013 ± 0.006	-0.079 ± 0.036
Low-extinction	12+log(O/H)	8.31 ± 0.05	0.006 ± 0.003	0.036 ± 0.018
All	12+log(Ar/H)	6.37 ± 0.04	-0.008 ± 0.002	-0.049 ± 0.012
High-extinction	12+log(Ar/H)	6.51 ± 0.08	-0.018 ± 0.006	-0.109 ± 0.036
Low-extinction	12+log(Ar/H)	6.3 ± 0.05	-0.005 ± 0.003	-0.03 ± 0.018

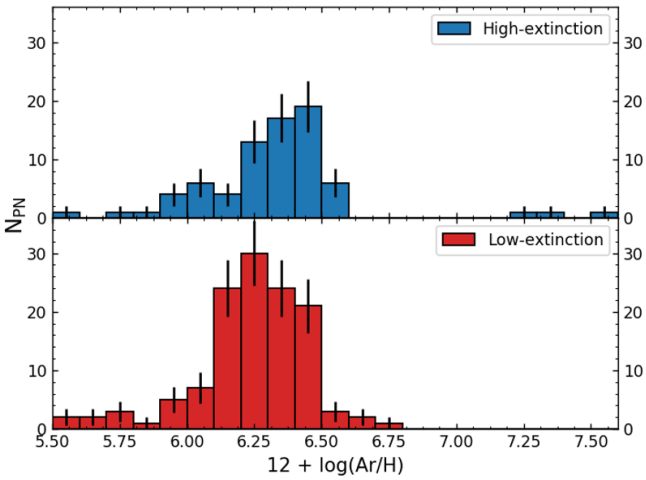

Figure 10. Histogram showing the distribution of argon abundances for the [top] high- and [bottom] low-extinction PNe. The bins are 0.1 dex wide, vertical bars indicate the Poissonian errors.

(2012) found that for HII regions the oxygen abundance gradient (determined indirectly for a large sample), $(\Delta(O/H)/\Delta R)_{HII-regions} = -0.023 \pm 0.002$ dex/kpc is steeper than that observed for either of the PN populations. However, we do find a similar intercept for the high-extinction PNe (12+log(O/H)$_{0,\ high-ext}$ = 8.6 ± 0.08) and the HII regions (12+log(O/H)$_{0,\ HII-regions}$ = 8.72 ± 0.18; Zurita & Bresolin 2012). Both high extinction PNe and HII regions show the highest oxygen abundance values at $R_{GC} < 5$ kpc.

3.2 Argon abundance distribution and radial gradient from Planetary Nebulae

Figure 10 shows the PN argon abundance distribution for the high- and low-extinction PNe in the M 31 disc within ~30 kpc. We utilize the AD-test to statistically compare the two distributions which yields a significance level of 3.3%. Since the significance level is lesser than 5%, the null hypothesis that the two samples are drawn from the same distribution is rejected. Thus the two disc components in M31 traced by the high- and low- extinction PNe have stellar populations that were born from ISM with distinct argon and oxygen abundance distributions. Their parent stellar populations, forming the thin and thicker disc of M 31, are not only kinematically distinct (Paper II), but also have distinct elemental abundances and radial gradients. The mean value of the argon abundance for the high-extinction PNe, $< 12 + \log(Ar/H) >_{high-ext} = 6.32 \pm 0.03$, is clearly higher than that for the low- extinction PNe, $< 12+\log(Ar/H) >_{low-ext} = 6.25 \pm 0.02$. The standard deviation values, $\sigma(12+\log(Ar/H))_{high-ext} = 0.29$ and

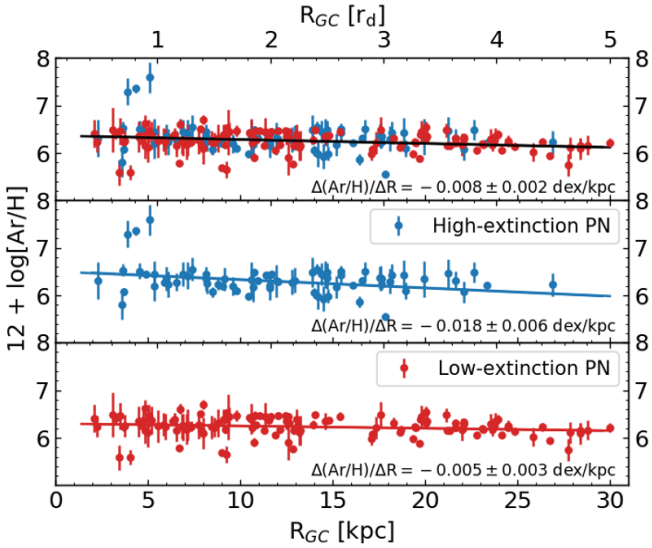

Figure 11. The galactocentric radial distribution of argon abundances for [top] all, [middle] high- and [bottom] low-extinction PNe in the M 31 disc in our *PN_M31d_O_lim* sample. The bottom and top axes show R_{GC} in units of kpc and r_d respectively. High- and low-extinction PNe are shown in blue and red respectively. The best-fitting radial argon abundance gradient to the *PN_M31d_O_lim* sample is shown for all (black), high- (blue) and low-extinction (red) PNe.

$\sigma(12 + \log(Ar/H))_{low-ext} = 0.2$, reflect an overlap of their argon abundance distribution.

Figure 11 shows the galactocentric radial distribution of PN argon abundances for the high- and low-extinction PNe samples in R_{GC} =2–30 kpc radial range. Their fitted parameters are also noted in Table 5. We find a steeply negative argon abundance gradient for the high-extinction PNe, $(\Delta(Ar/H)/\Delta R)_{high-ext} = -0.018 \pm 0.006$ dex/kpc while for all PNe and the low-extinction PNe we find negative and slightly negative argon abundance gradients respectively, $(\Delta(Ar/H)/\Delta R)_{all} = -0.008 \pm 0.002$ dex/kpc and $(\Delta(Ar/H)/\Delta R)_{low-ext} = -0.005 \pm 0.003$ dex/kpc.

We can then compare the argon abundance gradients in PNe with that of the oxygen abundance gradient computed for HII regions[4]. The high-extinction PNe have an abundance gradient which is consistent within error with that of the HII regions, $(\Delta(O/H)/\Delta R)_{HII-regions} = -0.023 \pm 0.002$ dex/kpc (Zurita & Bresolin 2012), implying that both the parent stellar populations of these young PNe and the HII regions originated from a similarly-enriched ISM. The near-flat abundance gradient of the low-extinction PNe, on the other hand, implies a parent stellar population which has a different chemical composition and radial trend.

[4] Direct determination of oxygen and argon abundances for HII regions has been carried out only for 16 HII regions (where the faint [O III] 4363 Å emission line is observed; Esteban et al. 2020) over a limited radial range. This small sample and limited radial range do not allow for a well constrained determination of radial oxygen and argon abundance gradient for HII regions in M 31. However, as mentioned in Section 3.1, a much larger sample of HII regions have oxygen abundances determined using strong line methods (Zurita & Bresolin 2012), giving a more robust estimate of the oxygen abundance gradient for HII regions in M 31, suitable for comparison with the gradients determined from PNe.

4 COMPARISON OF RADIAL ABUNDANCE GRADIENT FROM M 31 DISC PLANETARY NEBULAE WITH GRADIENTS IN GALAXY DISCS

4.1 Comparison with previous nebular abundance gradient estimates in the M 31 disc

Previous PN abundance gradient estimates in the M 31 disc (Sanders et al. 2012; Kwitter et al. 2012; Peña & Flores-Durán 2019) computed a flat radial oxygen abundance gradient out to large galactocentric radii. Peña & Flores-Durán (2019) found an oxygen abundance gradient of -0.001 ± 0.001 dex/kpc within R_{GC} ~110 kpc, including both disc and halo PNe and an argon abundance gradient of -0.002 ± 0.001 dex/kpc for the same sample. The flat oxygen abundance gradient determined in this work for all PNe (0.001 ± 0.003 dex/kpc; Table 5) is consistent with what was previously computed. Our derived radial argon abundance gradient for all PNe of -0.008 ± 0.002 dex/kpc within R_{GC} ~30 kpc is steeper than that observed by Peña & Flores-Durán (2019). Given their larger galactocentric radial range and smaller PNe sample size, coupled with fewer high-extinction PNe at large radii the comparison of their argon radial abundance gradient is more suitable with our derived argon radial abundance gradient for low-extinction PNe (-0.005 ± 0.003 dex/kpc). Both these values (ours and Peña & Flores-Durán 2019) are consistent within errors.

The previous PN abundance gradient estimates in the M 31 disc were in contrast to the steeper gradient computed from HII regions (Zurita & Bresolin 2012). By classifying PNe samples on the basis of their intrinsic extinction, we have identified that the younger, dynamically colder (Paper II), high-extinction PNe have a steeper radial oxygen abundance gradient which is consistent with that of the HII regions. We confirm that the older dynamically hotter low-extinction PNe have a flat oxygen abundance gradient that also drives the abundance gradient of all PNe jointly given their larger number.

4.2 Comparison with previous stellar metallicity gradients in the M 31 disc

We can compare the radial oxygen and argon abundance gradient to other stellar metallicity gradients derived in the M 31 disc. We decide to convert the argon abundance gradient to stellar metallicity as argon is unequivocally invariant during AGB evolution (see Appendix C for details). To facilitate comparison, the argon abundance is converted to [M/H] by subtracting the solar [Ar/H] value (=6.38; Asplund et al. 2021) as is done for calibrating stellar and gas phase mass–metallicity relations of galaxies (e.g., Zahid et al. 2017). This has no effect on the gradients. We now compare the metallicity gradient from PN argon abundances with other chemical information derived from stars in the M 31 disc from independent studies. Gregersen et al. (2015) found a metallicity gradient of -0.02 ± 0.004 dex/kpc from R_{GC} ~4–20 kpc in the M 31 disc in the PHAT survey. They assumed solar [α/Fe] and a constant red giant branch (RGB) age of 4 Gyr. Note that choosing a different age had consequences on the [M/H] intercept but the metallicity gradient remained unchanged within errors. Figure 12 shows the metallicity gradient found by Gregersen et al. (2015) in each panel. Their fitted stellar metallicity gradient is most similar to that of the high-extinction PNe, which are estimated to have a younger age of ~ 2.5 Gyr (Paper II). This implies that their RGB stars assumed to have a mean age of 4 Gyr, may be contaminated by younger stars. We further note that Saglia et al. (2018), from IFU observations of the M 31 central regions within R_{GC} ~5 kpc, found a [M/H] gradient of 0.0 ± 0.03 dex/kpc. Given the error, their gradient is consistent with that of both the high- and low- extinction PNe.

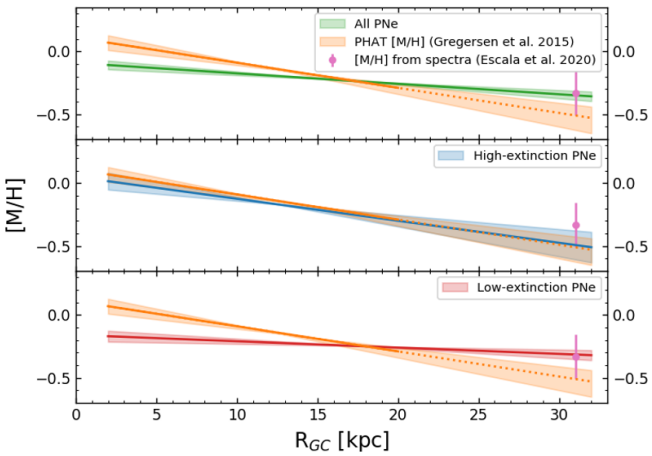

Figure 12. The best-fitting radial argon abundance gradient to the *PN_M31d_O_lim* sample, scaled to [M/H], is shown for [top] all, [middle] high- and [bottom] low-extinction PNe. In each panel, we show the best-fit radial gradient to the PHAT photometric metallicity (fitted to R_{GC} = 20 kpc by Gregersen et al. 2015, shown as a solid orange line, and extrapolated beyond as dotted line). The uncertainty in the fits are shaded. Also shown in each panel is the spectroscopic [M/H] obtained by Escala et al. (2020) for resolved RGB stars in a small field.

Escala et al. (2020) computed [Fe/H] and [α/Fe] values from individual stars in small field at R_{GC} ~31 kpc in the M 31 disc. Their mean [Fe/H] and [α/Fe] values in this field are converted to [M/H] using the relation from Salaris & Cassisi 2005 (see Appendix B in Paper III for details) to find their [M/H]=-0.33 ± 0.18. Since very few high-extinction PNe are expected to be found beyond 20 kpc radius (Paper II), it is likely that the [M/H] derived by Escala et al. (2020) corresponds to PNe in the older thicker disc, the same population probed by the low-extinction PNe. In fact, we can clearly see in Figure 12 that their spectroscopic [M/H] value is consistent with the metallicity value obtained from the argon abundance gradient for the low extinction PNe at these radii.

4.3 Comparison of PN radial abundance gradients of the Milky Way and M 31

Considering all available MW disc PNe, Stanghellini & Haywood (2018) derived radial oxygen and argon abundance gradients of -0.021 dex/kpc and -0.029 dex/kpc respectively. Adopting MW disc scale-length, r_d = 2.3 kpc from Yin et al. (2009), a suitable value within the range of disc scale-length measurements (Bland-Hawthorn & Gerhard 2016), this corresponds to oxygen and argon abundance gradients of -0.048 dex/r_d and -0.067 dex/r_d respectively. Adopting a M 31 disc scale length of r_d = 6.08 kpc (Yin et al. 2009), the oxygen and argon abundance gradients for all PNe in the *PN_M31d_O_lim* sample in this work have radial gradients of 0.006 ± 0.018 dex/r_d and -0.049 ± 0.018 dex/r_d respectively. These are noted in Table 5 along with those of other sub-samples calculated previously. In both the MW and M 31, PNe have flatter oxygen abundance gradients than argon ones but the oxygen abundance gradient is much flatter in M 31 than in the MW. The argon radial abundance gradient in M 31 is also consistent with that of the MW within errors.

Stanghellini & Haywood (2018) separately probed the thin and thick disc of the MW using younger (<1 Gyr; YPPNe) and older (>7 Gyr; OPPNe) PNe respectively. Their YPPNe exclusively populated the MW thin disc while the OPPNe had a parent stellar population

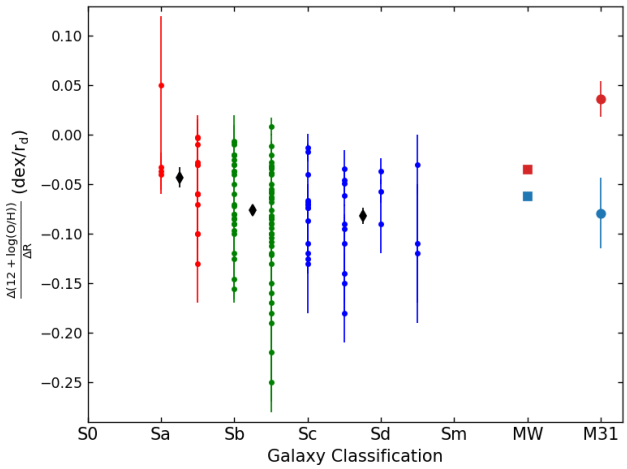

Figure 13. The oxygen radial abundance gradients derived in terms of disc scale length for galaxies of different morphological types in Sánchez-Menguiano et al. (2016). The Sa-Sab (red), Sb-Sbc (green) and Sc-Sdm (dark blue) galaxies also have their mean oxygen abundance gradients plotted in black. The oxygen abundance gradients for the MW (Stanghellini & Haywood 2018) (square symbols) and M 31 (this work, larger dots) are marked. The MW and M 31 thin disc values are marked in light blue while that for the MW thick disc and the M 31 thicker disc are marked in red.

dominated by thick disc stars with some contribution from old thin disc stars. They found that the YPPNe and the OPPNe had oxygen abundance gradients (in their selected sample; see their Table 4) of −0.027 dex/kpc and −0.015 dex/kpc respectively. In terms of disc scale lengths, YPPNe and the OPPNe would have oxygen abundance gradients of −0.062 dex/r_d and −0.035 dex/r_d respectively, marked in Figure 13. These can be compared to the oxygen abundance gradients in M 31 (see Table 5 and the marked values in Figure 13). The high-extinction PNe in M 31 (with ages ∼ 2.5 Gyr; Paper II) have a gradient in remarkable agreement with that of the YPPNe in the MW. The low-extinction PNe (with ages ∼4.5 Gyr; Paper II) have a positive near-flat gradient, which differs from the negative gradient of the OPPNe in the MW. The positive gradient in the M 31 thicker disc may be the end result from a major-merger event, to be discussed later in Section 5.1.

4.4 Comparison with radial abundance gradients of other galaxies

Sánchez-Menguiano et al. (2016) computed the oxygen abundance profiles in a sample of 122 face-on spiral galaxies observed by the CALIFA IFU survey(Sánchez et al. 2012) using both binned spaxels and individually identified HII regions[5]. Figure 13 shows the oxygen abundance gradients in terms of disc scale length for galaxies of different morphological types in their sample. Sa–Sab type galaxies that have the least prominent spiral arms with lowest star-formation, also show the flattest radial oxygen gradients. Other morphological types of spiral galaxies (Sb–Sdm) in the CALIFA sample have relatively steeper abundance gradients with a mean of −0.07 dex/r_d. Such individual spirals span a wide range of radial oxygen gradients values, with many having near-flat gradients like those of the MW thick disc, while several others having steeper slopes than that observed for the MW and M 31 thin disc. However, the thicker disc of M 31 has a positive radial oxygen gradient comparable only to one such value for a Sa-type galaxy in the CALIFA sample, being flatter than any of those for the Sab–Sdm type galaxies.

5 CONSTRAINTS ON THE FORMATION HISTORY OF THE M 31 DISC

5.1 Inferences on chemical evolution of galaxies from radial abundance gradients

Simulations of chemical evolution in isolated galaxies make predictions on the variation of the radial abundance gradient over time depending on the choice of physical mechanisms, particularly feedback prescriptions, that govern the enrichment of elements into the ISM (e.g. Gibson et al. 2013; Mollá et al. 2019). Such simulations generally predict either an initial flat gradient that steepens over time or an initial steep one that flattens over time (Gibson et al. 2013; Mollá et al. 2019). One can attempt to constrain such models by comparing with radial abundance gradients of stars formed at different epochs in a galaxy, as carried out using the PNe, HII regions and other stellar tracers in the MW by Stanghellini & Haywood (2018) and Mollá et al. (2019).

To constrain the chemical evolution of galaxies from chemical abundance gradients, estimates are required for at least two epochs. The gradients for the high and low extinction PN samples provide estimates in M 31 for two distinct but relatively broad age ranges, ∼2.5 Gyr and ∼4.5 Gyr and older respectively. A third epoch for such a comparisons, the present-day epoch, is provided by the oxygen abundance gradient in the M 31 HII regions. The thicker disc PNe (corresponding to a redshift, z∼0.5) have a flatter abundance gradient than the thin disc PNe or the HII regions. The chemical evolution models of isolated galaxies in Mollá et al. (2019) predict a gradient of −0.0106 ± 0.0010 dex/kpc (or −0.053 ± 0.005 dex/r_d) for the MW at z∼0.5 (Gibson et al. 2013 predict −0.04 dex/r_d for the same), much steeper than the observed positive radial gradient (0.036 ± 0.018 dex/r_d) of the M 31 thicker disc. In fact, such a positive radial gradient is not predicted in any models of chemical evolution for isolated disc galaxies covering a wide range of total masses (Mollá & Díaz 2005), which have their flattest radial oxygen gradient at −0.01 dex/r_d. [6]

5.2 Radial migration as a driver for the flat oxygen gradient in the M31 thicker disc

Magrini et al. (2016) noted that the radial oxygen abundance gradient

[5] We note that an updated study of galaxy properties from an expanded CALIFA IFU survey has been presented by Espinosa-Ponce et al. (2022). However, they do not provide the oxygen abundance gradient of individual galaxies in their sample but only their mean properties as a function of mass and morphological classification, which are in broad agreement with the results of Sánchez-Menguiano et al. (2016). As seen in Figure 13, the diversity of galaxy radial oxygen abundance gradients is not entirely captured by their mean values. For a meaningful comparison to the oxygen abundance gradient of the MW and M 31, individual galaxy oxygen abundance gradients are required with any binned sample needing to take the properties of the MW and M 31 into account. We therefore limit our comparison to the smaller CALIFA sample of Sánchez-Menguiano et al. (2016).

[6] The radial oxygen gradient of the M 31 thin disc (−0.079 ± 0.036 dex/r_d) is comparable with that of chemical evolution models of MW-type isolated galaxies (−0.1 dex/r_d; Mollá et al. 2019).

of the M 31 PNe derived from the entire sample of Sanders et al. (2012) was flatter than the predictions from the chemical evolution models of isolated galaxies by Mollá & Díaz (2005). Since such models do not account for the dynamical effects of secular evolution, Magrini et al. (2016) attributed the flat radial oxygen abundance gradient in the M 31 disc to radial migration. Radial migration, possibly induced by bar resonances and transient spiral arms, may displace stars from their birth positions to larger radii thereby flattening the radial abundance gradient (Roškar et al. 2008; Minchev et al. 2011).

Is then radial migration a possible explanation for the positive abundance gradient of the M31 thicker disc? If we were to focus only on the redistribution of stars at larger radii, then indeed radial migration brings about a flattening of the abundance gradient. According to Sellwood (2014) such secular processes do not dynamically heat the disc though, and thus one can not reproduce the observed high rotational velocity dispersion (σ_ϕ = 101 ± 13 km s^{-1}; Paper II) of the thicker disc PNe, which would then be left unexplained.

Since merger events do flatten the radial metallicity gradients of pre-merger discs (Zinchenko et al. 2015) and can heat the discs (Quinn & Goodman 1986), the derived flatter (even positive for oxygen) abundance gradients of the M 31 thicker and dynamically hot disc, compared to that from chemical evolution models of isolated discs, shows the influence of the recent merger on the radial metallicity gradient of M 31. It is further explored in the next section.

5.3 The radial elemental abundance gradient in galaxy merger simulations and the merger scenario in M 31

N-body simulations of interacting galaxies have shown that mergers leave imprints on the metallicity gradient of a galaxy, including dilution of the concentration of metals in the central part of galaxies due to gas inflow during initial passages as well as flattening of the radial metallicity gradient during the interaction (Rupke et al. 2010; Zinchenko et al. 2015). A near-flat abundance gradient has also been seen in EAGLE cosmological simulations of disc galaxies which experienced mergers with mass ratio ≥1:10 (Tissera et al. 2019).

In a minor merger scenario in M 31 as advocated by Fardal et al. (2013), a satellite galaxy (mass ratio ∼ 1:20) infalls along the giant stream on to the M 31 disc ∼1 Gyr ago. Such a satellite however would not be able to produce a heated disc with the velocity dispersion of 100 km s^{-1} as measured in Paper II for the low-extinction PNe in M 31 and would additionally not form a distinct hot thin disc (Martig et al. 2014). Following the major merger scenario described by Hammer et al. (2018), however, the pre-merger disc in M 31 would be perturbed by the a massive satellite (mass ratio > 1:4.5) in a highly retrograde orbit. A prediction of this merger model is that a thin disk is rebuilt from the gas brought in by the satellite along with a burst of star formation following the dissolution of said satellite.

Zinchenko et al. (2015) quantified the effect of mergers on the radial elemental abundance profiles of MW mass galaxies using N-body simulations (no new star formation). They found that the amount of flattening of the radial abundance gradient at large radii depends on the mass and inclination of the in-falling satellite, with flatter gradients observed for the more massive mergers. They find the maximum possible flattening from ∼1:20 and ∼1:6 mergers are 0.041 dex/r$_d$ and 0.067 dex/r$_d$ respectively which occur for prograde mergers. We can check the flattening of the radial oxygen abundance gradient if we assume that the pre-merger thicker disc of M 31 had a radial oxygen abundance gradient similar to that of the MW (−0.035 dex/r$_d$), a reasonable assumption given the thin discs of the two galaxies have similar radial gradients (see Section 4.3). Then the M 31 thicker disc gradient was flattened by 0.071 dex/r$_d$, consistent with a mass ratio of the merger event in M 31 of at least ∼1:6 or larger depending on the orbital inclination of the infalling satellite.

The observed high-extinction PNe are ∼2.5 Gyr old (or younger; Paper II) and likely trace the thin disc during its formation. The chemical evolution of an isolated thin disc after its formation has been shown in other hydrodynamic models (e.g. Mollá et al. 2019) to result in a negative radial abundance gradient, consistent with the observed negative abundance gradient for the thin disc high-extinction PNe. Furthermore, Vincenzo & Kobayashi (2020) show that a starburst following gas in-fall into a galaxy at large radii can steepen the metallicity gradient of stars formed after the in-fall. In the case of M 31, the steep thin disc radial oxygen and argon abundance gradients are consistent with the thin disc having formed in a starburst event from less enriched gas brought in by the satellite mixed with the enriched ISM in the pre-merger M31 disc within R$_{GC}$ = 14 kpc[7] (Paper V). The stars in the thin disc at R$_{GC}$ > 18 kpc are formed in a starburst event predominantly from the satellite gas (Paper V). The dilution of the ISM in the M 31 disc from the accreted satellite gas is consistent with the low stellar metallicity (Conn et al. 2016; Cohen et al. 2018) of the giant stream substructure, which is the remaining stellar trail left by the satellite. In this context, see the recent results on the giant stream metallicity distribution from N-body simulations by Milošević et al. (2022).

The elemental abundance gradient from PNe thus acts as constraints for merger-induced chemical evolution simulations in galaxies in general and M 31 in particular. While the fairly major merger simulations by Hammer et al. (2018) do predict the formation of distinct thin and thick discs as observed, predictions of the abundance gradients from such simulations (not explicitly predicted in Hammer et al. 2018) must be constrained in future investigations using the current values derived for the ISM using PNe.

6 CONCLUSIONS

We present the largest sample of PNe in the M 31 disc with extinction measurements, oxygen abundances and argon abundances. We classify our observed PNe on the basis of their measured extinction. Oxygen and argon abundance distributions and radial gradients are derived for the high- and low-extinction PNe separately in the M 31 disc from direct temperature measurements. The high- and low- extinction PN abundance gradients trace the younger thin and older thicker disc of M 31 respectively. Our conclusions can be summarised as follows:

- Comparing the oxygen and argon abundances in the thin and thicker discs of M 31 reveals that the two discs have distinct abundance distributions. This is the first evidence of chemically distinct thin and thicker discs in M 31.
- We find a steeper radial abundance gradient for the thin disc of M 31 (consistent with that of HII regions) and a near-flat (slightly positive for oxygen and slightly negative for argon) abundance gradient for the thicker disc. This is also consistent with the findings of previous studies whose near-flat PN abundance gradient estimates were dominated by the more numerous low-extinction PNe.
- The steep abundance gradient of the M 31 thin disc is consistent with the younger thin disc having been formed following a wet merger event. The chemical enrichment history of the thin and thicker

[7] For details see the galactic chemical evolution models for the inner M 31 disc, presented in Paper V, with the loop in the log(O/Ar) vs. 12+log(A/H) plane for the young higher extinction PNe at this radii.

disc of M 31 has been explored in Paper V through the log(O/Ar) vs 12+log(Ar/H) plane, using the oxygen and argon abundances determined in this work. There we found the M 31 thicker disc had an extended star-formation history while the thin disc formed in a burst of star-formation following a wet merger event with metal-poor gas brought in by the satellite.

- The thin discs of the MW and M 31 have remarkably similar oxygen abundance gradients when difference in their disc-scale lengths is taken into account.
- The abundance gradients for the thicker disc is flatter than expected from chemical evolution models of isolated galaxies but are consistent with the expectations of a major merger scenario (mass ratio ~1:5; Paper II). The oxygen abundance gradient of the M 31 thicker disc, in particular, is amongst the most positive observed till date in spiral galaxies, much more positive than that of the MW thick disc. The chemical abundance of the M 31 thicker disc has been radially homogenised as a consequence of the merger event. Given that the merger mass and orbital inclination has measurable influence on the metallicity gradient (Zinchenko et al. 2015), the observed abundance gradients can provide constraints on the mass and inclination of the merging satellite in a major-merger scenario in M 31.

ACKNOWLEDGEMENTS

We thank the anonymous referee for their comments. SB acknowledges support from the European Southern Observatory (ESO), Garching, Germany during his PhD. A preliminary version of this work appears in his PhD thesis (Bhattacharya 2020). SB is funded by the INSPIRE Faculty award (DST/INSPIRE/04/2020/002224), Department of Science and Technology (DST), Government of India. MAR and SB thank ESO for supporting SB's visit through the 2021 ESO SSDF. MAR, SB and OG are grateful for the hospitality of the Mount Stromlo Observatory and the Australian National University (ANU). MAR and OG thank the Research School of Astronomy and Astrophysics at ANU for support through their Distinguished Visitor Program. This work was supported by the DAAD under the Australia-Germany joint research program with funds from the German Federal Ministry for Education and Research. CK acknowledges funding from the UK Science and Technology Facility Council through grants ST/R000905/1 and ST/V000632/1. Based on observations obtained at the MMT Observatory, a joint facility of the Smithsonian Institution and the University of Arizona. Based on observations obtained with MegaPrime/MegaCam, a joint project of CFHT and CEA/DAPNIA, at the Canada-France-Hawaii Telescope (CFHT). This research made use of Astropy– a community-developed core Python package for Astronomy (Astropy Collaboration et al. 2013), SciPy (Virtanen et al. 2019), NumPy (Oliphant 2015) and Matplotlib (Hunter 2007). This research also made use of NASA's Astrophysics Data System (ADS[8]).

DATA AVAILABILITY

Tables 3 and B1 provide the required data on the kinematics and chemical abundances of the M 31 *PN_M31d_O_lim* PN sample and will be made available in full through the CDS. The PN spectra can be shared upon reasonable request to the authors.

[8] https://ui.adsabs.harvard.edu

REFERENCES

Aniyan S., et al., 2018, MNRAS, 476, 1909
Aniyan S., Ponomareva A. A., Freeman K. C., Arnaboldi M., Gerhard O. E., Coccato L., Kuijken K., Merrifield M., 2021, MNRAS, 500, 3579
Arnaboldi M., et al., 2022, arXiv e-prints, p. arXiv:2208.02328
Asplund M., Amarsi A. M., Grevesse N., 2021, A&A, 653, A141
Astropy Collaboration et al., 2013, A&A, 558, A33
Belokurov V., Erkal D., Evans N. W., Koposov S. E., Deason A. J., 2018, MNRAS, 478, 611
Bhattacharya S., 2020, PhD thesis, Ludwig-Maximilians University of Munich, Germany, doi:10.5282/edoc.27186
Bhattacharya S., Arnaboldi M., Hartke J., Gerhard O., Comte V., McConnachie A., Caldwell N., 2019a, A&A, 624, A132
Bhattacharya S., et al., 2019b, A&A, 631, A56
Bhattacharya S., Arnaboldi M., Gerhard O., McConnachie A., Caldwell N., Hartke J., Freeman K. C., 2021, A&A, 647, A130
Bland-Hawthorn J., Gerhard O., 2016, Annual Review of Astronomy and Astrophysics, 54, 529
Bresolin F., Stasińska G., Vílchez J. M., Simon J. D., Rosolowsky E., 2010, MNRAS, 404, 1679
Brook C. B., Kawata D., Gibson B. K., Freeman K. C., 2004, ApJ, 612, 894
Bullock J. S., Johnston K. V., 2005, ApJ, 635, 931
Caldwell N., Harding P., Morrison H., Rose J. A., Schiavon R., Kriessler J., 2009, AJ, 137, 94
Cardelli J. A., Clayton G. C., Mathis J. S., 1989, ApJ, 345, 245
Ciardullo R., Jacoby G. H., 1999, ApJ, 515, 191
Ciardullo R., Feldmeier J. J., Jacoby G. H., Kuzio de Naray R., Laychak M. B., Durrell P. R., 2002, ApJ, 577, 31
Coccato L., et al., 2009, MNRAS, 394, 1249
Cohen R. E., et al., 2018, AJ, 156, 230
Collins M. L. M., et al., 2011, MNRAS, 413, 1548
Comerón S., Salo H., Knapen J. H., Peletier R. F., 2019, A&A, 623, A89
Conn A. R., et al., 2016, MNRAS, 458, 3282
Corradi R. L. M., Kwitter K. B., Balick B., Henry R. B. C., Hensley K., 2015, ApJ, 807, 181
Cortesi A., et al., 2013, A&A, 549, A115
Dalcanton J. J., et al., 2012, The Astrophysical Journal Supplement Series, 200, 18
Delgado-Inglada G., Morisset C., Stasińska G., 2014, MNRAS, 440, 536
Delgado-Inglada G., Rodríguez M., Peimbert M., Stasińska G., Morisset C., 2015, MNRAS, 449, 1797
Dorman C. E., et al., 2015, ApJ, 803, 24
Escala I., Gilbert K. M., Kirby E. N., Wojno J., Cunningham E. C., Guhathakurta P., 2020, ApJ, 889, 177
Espinosa-Ponce C., Sánchez S. F., Morisset C., Barrera-Ballesteros J. K., Galbany L., García-Benito R., Lacerda E. A. D., Mast D., 2022, MNRAS, 512, 3436
Esteban C., Bresolin F., García-Rojas J., Toribio San Cipriano L., 2020, MNRAS, 491, 2137
Fabricant D., et al., 2005, Publications of the Astronomical Society of the Pacific, 117, 1411
Fang X., Zhang Y., García-Benito R., Liu X. W., Yuan H. B., 2013, ApJ, 774, 138
Fang X., García-Benito R., Guerrero M. A., Liu X., Yuan H., Zhang Y., Zhang B., 2015, ApJ, 815, 69
Fang X., et al., 2018, ApJ, 853, 50
Fardal M. A., et al., 2013, MNRAS, 434, 2779
Ferland G. J., Korista K. T., Verner D. A., Ferguson J. W., Kingdon J. B., Verner E. M., 1998, Publications of the Astronomical Society of the Pacific, 110, 761
García-Hernández D. A., Górny S. K., 2014, A&A, 567, A12
García-Hernández D. A., Ventura P., Delgado-Inglada G., Dell'Agli F., Di Criscienzo M., Yagüe A., 2016, MNRAS, 458, L118
García-Rojas J., Peña M., Flores-Durán S., Hernández-Martínez L., 2016, A&A, 586, A59
Gibson B. K., Pilkington K., Brook C. B., Stinson G. S., Bailin J., 2013, A&A, 554, A47

Gilmore G., Reid N., 1983, MNRAS, 202, 1025
Gregersen D., et al., 2015, AJ, 150, 189
Guhathakurta P., Ostheimer J. C., Gilbert K. M., Rich R. M., Majewski S. R., Kalirai J. S., Reitzel D. B., Patterson R. J., 2005, arXiv e-prints [astro-ph/0502366]
Hammer F., Yang Y. B., Wang J. L., Ibata R., Flores H., Puech M., 2018, MNRAS, 475, 2754
Hartke J., et al., 2018, A&A, 616, A123
Hartke J., et al., 2022, arXiv e-prints, p. arXiv:2201.08710
Helmi A., Babusiaux C., Koppelman H. H., Massari D., Veljanoski J., Brown A. G. A., 2018, Nature, 563, 85
Hernández-Martínez L., Carigi L., Peña M., Peimbert M., 2011, A&A, 535, A118
Herrmann K. A., Ciardullo R., Feldmeier J. J., Vinciguerra M., 2008, ApJ, 683, 630
Hopkins P. F., Cox T. J., Younger J. D., Hernquist L., 2009, ApJ, 691, 1168
Hunter J. D., 2007, Computing In Science & Engineering, 9, 90
Kingsburgh R. L., Barlow M. J., 1994, MNRAS, 271, 257
Kobayashi C., Karakas A. I., Lugaro M., 2020, ApJ, 900, 179
Kreckel K., Groves B., Bigiel F., Blanc G. A., Kruijssen J. M. D., Hughes A., Schruba A., Schinnerer E., 2017, ApJ, 834, 174
Kwitter K. B., Henry R. B. C., 2021, arXiv e-prints, p. arXiv:2110.13993
Kwitter K. B., Lehman E. M. M., Balick B., Henry R. B. C., 2012, ApJ, 753, 12
Liu X. W., Storey P. J., Barlow M. J., Danziger I. J., Cohen M., Bryce M., 2000, MNRAS, 312, 585
Maciel W. J., Koppen J., 1994, A&A, 282, 436
Magrini L., Coccato L., Stanghellini L., Casasola V., Galli D., 2016, A&A, 588, A91
Martig M., Minchev I., Flynn C., 2014, MNRAS, 443, 2452
McConnachie A. W., et al., 2009, Nature, 461, 66
McConnachie A. W., et al., 2018, ApJ, 868, 55
Merrett H. R., et al., 2003, MNRAS, 346, L62
Merrett H. R., et al., 2006, MNRAS, 369, 120
Miller Bertolami M. M., 2016, A&A, 588, A25
Milošević S., Mićić M., Lewis G. F., 2022, MNRAS,
Minchev I., Famaey B., Combes F., Di Matteo P., Mouhcine M., Wozniak H., 2011, A&A, 527, A147
Mollá M., Díaz A. I., 2005, MNRAS, 358, 521
Mollá M., Díaz Á. I., Cavichia O., Gibson B. K., Maciel W. J., Costa R. D. D., Ascasibar Y., Few C. G., 2019, MNRAS, 482, 3071
Morisset C., 2017, in Liu X., Stanghellini L., Karakas A., eds, Vol. 323, Planetary Nebulae: Multi-Wavelength Probes of Stellar and Galactic Evolution. pp 43–50 (arXiv:1612.04242), doi:10.1017/S1743921317001004
Oliphant T. E., 2015, Guide to NumPy, 2nd edn. CreateSpace Independent Publishing Platform, USA
Peña M., Flores-Durán S. N., 2019, Rev. Mex. Astron. Astrofis., 55, 255
Peñarrubia J., McConnachie A., Babul A., 2006, ApJ, 650, L33
Pulsoni C., et al., 2018, A&A, 618, A94
Quinn P. J., Goodman J., 1986, ApJ, 309, 472
Roškar R., Debattista V. P., Quinn T. R., Stinson G. S., Wadsley J., 2008, ApJ, 684, L79
Rupke D. S. N., Kewley L. J., Barnes J. E., 2010, ApJ, 710, L156
Sadoun R., Mohayaee R., Colin J., 2014, MNRAS, 442, 160
Saglia R. P., Opitsch M., Fabricius M. H., Bender R., Blaña M., Gerhard O., 2018, A&A, 618, A156
Salaris M., Cassisi S., 2005, Evolution of Stars and Stellar Populations
Sánchez-Menguiano L., et al., 2016, A&A, 587, A70
Sánchez-Menguiano L., et al., 2018, A&A, 609, A119
Sánchez S. F., et al., 2012, A&A, 538, A8
Sanders N. E., Caldwell N., McDowell J., Harding P., 2012, ApJ, 758, 133
Schlegel D. J., Finkbeiner D. P., Davis M., 1998, ApJ, 500, 525
Scholz F. W., Stephens M. A., 1987, Journal of the American Statistical Association, 82, 918
Sellwood J. A., 2014, Reviews of Modern Physics, 86, 1
Stanghellini L., Haywood M., 2018, ApJ, 862, 45
Stanghellini L., Magrini L., Casasola V., Villaver E., 2014, A&A, 567, A88

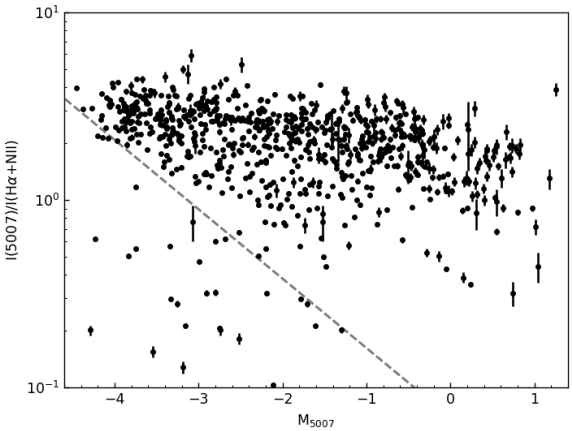

Figure A1. The ratio of foreground extinction corrected fluxes of [O III] 5007 Å and H-α+NII for the PNe candidates, where the NII flux is assumed to be its maximum value of half the H-α flux. The dashed line separates HII regions from PNe.

Tissera P. B., Rosas-Guevara Y., Bower R. G., Crain R. A., del P Lagos C., Schaller M., Schaye J., Theuns T., 2019, MNRAS, 482, 2208
Ventura P., Dell'Agli F., Schneider R., Di Criscienzo M., Rossi C., La Franca F., Gallerani S., Valiante R., 2014, MNRAS, 439, 977
Ventura P., Stanghellini L., Dell'Agli F., García-Hernández D. A., 2017, MNRAS, 471, 4648
Vincenzo F., Kobayashi C., 2020, MNRAS, 496, 80
Virtanen P., et al., 2019, arXiv e-prints, p. arXiv:1907.10121
Wesson R., 2016, MNRAS, 456, 3774
Wesson R., Stock D. J., Scicluna P., 2012, MNRAS, 422, 3516
White S. D. M., Rees M. J., 1978, MNRAS, 183, 341
Wilson E. B., 1927, Journal of the American Statistical Association, 22, 209
Yin J., Hou J. L., Prantzos N., Boissier S., Chang R. X., Shen S. Y., Zhang B., 2009, A&A, 505, 497
Yoachim P., Dalcanton J. J., 2006, AJ, 131, 226
Yoachim P., Dalcanton J. J., 2008a, ApJ, 682, 1004
Yoachim P., Dalcanton J. J., 2008b, ApJ, 683, 707
Zahid H. J., Kudritzki R.-P., Conroy C., Andrews B., Ho I. T., 2017, ApJ, 847, 18
Zinchenko I. A., Berczik P., Grebel E. K., Pilyugin L. S., Just A., 2015, ApJ, 806, 267
Zurita A., Bresolin F., 2012, MNRAS, 427, 1463

APPENDIX A: HII REGION CONTAMINATION

The PNe are identified in Paper I (and later in Paper III) as point-like sources bright in the [O III] narrow-band but faint in the broad g-band. With the high angular resolution of Megacam coupled with good seeing conditions, most HII regions at the distance of M 31 appear extended, as verified from HST observations (PHAT Dalcanton et al. 2012) in the M 31 disc in Paper I. However, contamination from ultra-compact HII regions (of radius < 10 pc) is still possible. From the PN spectra, we can distinguish between PNe and HII regions following the method described by Ciardullo et al. (2002) and Herrmann et al. (2008) using the flux ratio of the [O III] 5007 Å and H-α line (and NII which can be a maximum of 50% of the H-α line; Kreckel et al. 2017) as a function of absolute magnitude. For the candidate PNe identified in this work and including the archival sample from Sanders et al. (2012), we plot in Figure A1 the aforementioned line

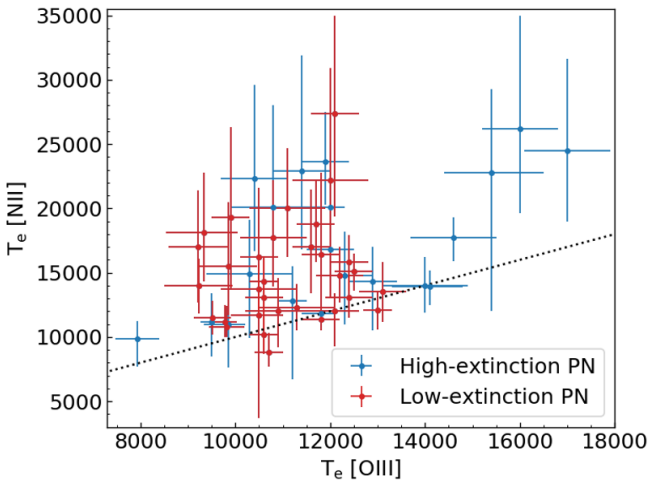

Figure B1. Comparison of the direct [O III]-based temperature with the direct [N II]-based temperature for those 52 PNe studied in this work where the [N II] 5755 Å line flux has been measured. High- and low-extinction PNe are marked separately. The dotted line shows the 1:1 line.

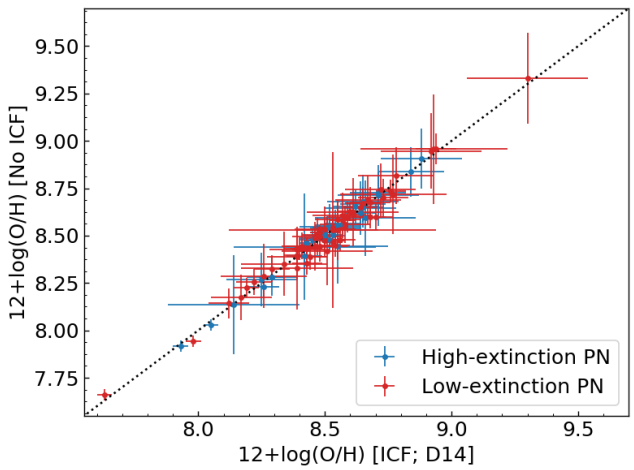

Figure B2. For a sub-sample of PNe where He I and He II recombination lines are observed, we compare the oxygen abundance determined by NEAT following the ICF scheme of Delgado-Inglada et al. (2014) and compare with the oxygen abundance determined assuming no ICF correction. High- and low-extinction PNe are marked separately. The dotted line shows the 1:1 line.

ratio, corrected for foreground extinction (A_V = 0.19 mag; Schlegel et al. 1998), against the absolute narrow-band magnitude, M_{5007} observed in Paper I for the distance (773 kpc; Conn et al. 2016) and foreground extinction of M31. The dashed line shows the selection criteria for PNe described by Ciardullo et al. (2002) and Herrmann et al. (2008), the region below which is occupied by HII regions. Thirty of the [O III] emitting sources may be classified as HII regions by this criteria. The remaining 1251 candidates are bonafide PNe.

APPENDIX B: FLUX MEASUREMENTS AND ABUNDANCE ESTIMATES

B1 Measured line fluxes

The measured line fluxes for the PNe in the *PN_M31d_O_lim* sample are noted in Table B1.

B2 Comparing direct temperature from [O III] and [N II]

The complete sample of 205 PNe studied in this work have flux measurements of the temperature-sensitive [O III] 4363 Å line, thereby allowing for direct [O III]-based temperature (T_e [O III]) determination. Of these PNe, 52 also have flux measurements of the temperature-sensitive [N II] 5755 Å line, thereby allowing for direct [N II]-based temperature (T_e [N II]) determination. Figure B1 shows the comparison of the (T_e [O III]) and (T_e [N II]) for these 52 PNe. Note that the mean error on T_e [O III] is 557 K compared to the 3598 K for T_e [N II], a consequence of the [N II] 5755 Å line being fainter with higher uncertainty on its determined flux. While a number of PNe lie on the 1:1 line, a number of them have higher (T_e [N II]) compared to their (T_e [O III]) estimate. However, the PNe which do not lie on the 1:1 line (within error) have higher mean uncertainty on the T_e [N II] of 4589 K compared to those on the 1:1 line with a mean uncertainty of 3217 K, implying that only the more uncertain T_e [N II] values do not lie on the 1:1 line. Furthermore, no difference in noted between the high- and low- extinction PNe in Figure B1.

A physical contribution towards higher T_e [N II] values compared to T_e [O III] could be the presence of high density clumps in PNe (Morisset 2017). At high densities, emission of the [N II] 6548, 6583 AA nebular lines can be suppressed due to collisional de-excitation (while emission of the [N II] 5755 Å auroral line is unaffected), and consequently T_e [N II] is overestimated (Fang et al. 2018). Another reason for the overestimated T_e [N II] values can be the recombination excitation of the [N II] 5755 Å line (Liu et al. 2000) which can not be corrected for in distant extragalactic PNe (due to the intrinsically faint and hence unobserved recombination lines). However, such recombination contribution affects the T_e [O III] by less than 1% (Liu et al. 2000).

Being unaffected by the presence of high-density clumps and recombination lines, T_e [O III] when measurable should be preferred for PN electron temperature estimation. Thus combined with its availability for the entire sample of PNe studied in this work, the lower uncertainty and inherent reliability , we utilise T_e [O III] for computing chemical abundances in this work.

B3 ICF correction for oxygen and argon abundance determination

Ionic abundances of O^+ and O^{++} are estimated from observed [O II] 3726/3729 Å and [O III] 4363/4959/5007 Å line fluxes respectively. However, estimation of oxygen abundances may require correction for unobserved O^{+3} ions. This can be achieved through the ICFs described by Delgado-Inglada et al. (2014) but that requires ionic abundance measurement of He^+ and He^{++}, which in turn requires observations of the relevant He I and He II recombination lines. While such lines are observed for 86 of our 205 PNe, for the rest of our sample they remain unobserved. For these 86 PNe, Figure B2 shows the oxygen abundance determined by NEAT following the ICF described by Delgado-Inglada et al. (2014) against the oxygen abundance assuming no ICF correction for these PNe. As seen from Figure B2, all points lie on the 1:1 line, within errors, thus the two abundance determination prescriptions lead to nearly identical oxygen abundance values. The ICF correction for unobserved O^{+3} ions is thus negligible in our sample, as was also found by Fang et al. (2018) with deeper spectra of M 31 PNe. It is to be noted that the

Table B1. Measured line fluxes of the 205 M31 PNe in the *PN_M31d_O_lim* sample. Column 1 shows the Sl. No. of the PN in this work while the latter columns refer to the observed flux of different emission lines, relative to Hβ=100. Following IAU naming conventions, each PN should be designated as SPNA<Sl. No.>. E.g. PN 478 should be termed SPNA478. A portion of this table is shown here for guidance; the full table will be made available through the CDS.

Sl. No.	[O II] 3726 Å	[O II] 3729 Å	H δ 4102 Å	H γ 4340 Å	[O III] 4363 Å	[Ar IV] 4711 Å	[Ar IV] 4740 Å	[O III] 4959 Å	[O III] 5007 Å	H α 6562 Å	[S II] 6717 Å	[S II] 6731 Å	[Ar V] 7005 Å	[Ar III] 7136 Å	[Ar III] 7751 Å
478	17.7 ± 4.9	18.8 ± 4.8	19.3 ± 2.5	17.4 ± 1.6	15.0 ± 1.2	–	5.1 ± 1.3	581.9 ± 6.6	1753.9 ± 18.0	428.0 ± 6.2	–	–	–	28.0 ± 1.7	16.3 ± 16.3
496	36.7 ± 4.5	36.1 ± 4.6	22.7 ± 2.3	27.1 ± 1.9	17.3 ± 1.5	5.9 ± 1.4	8.1 ± 1.2	600.7 ± 7.8	1792.4 ± 21.7	331.1 ± 10.2	5.1 ± 1.1	9.2 ± 1.0	–	25.2 ± 1.4	15.1 ± 15.1
942	–	–	28.1 ± 1.1	25.5 ± 0.8	8.2 ± 1.0	–	–	309.6 ± 3.9	963.3 ± 13.6	296.3 ± 3.7	–	–	–	10.5 ± 0.2	5.4 ± 5.4
945	32.1 ± 2.4	21.8 ± 2.4	–	34.8 ± 1.1	8.3 ± 0.6	–	1.5 ± 0.3	366.9 ± 3.5	1105.7 ± 13.7	277.5 ± 4.4	2.1 ± 0.2	3.2 ± 0.3	–	12.8 ± 0.4	6.9 ± 6.9
959	34.0 ± 2.0	19.8 ± 2.3	–	20.2 ± 0.8	8.5 ± 0.6	–	–	455.7 ± 5.1	1339.6 ± 13.9	311.3 ± 5.8	1.9 ± 0.3	3.9 ± 0.4	–	14.5 ± 0.4	7.3 ± 7.3

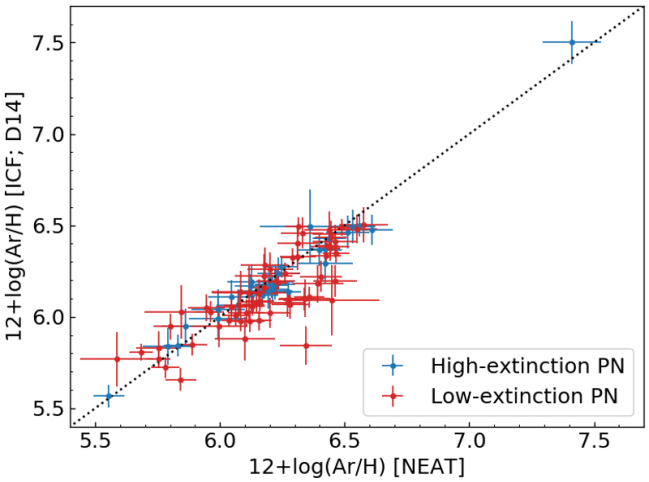

Figure B3. For a sub-sample of PNe where multiple argon ionic abundances have been determined, we compare the argon abundance determined by NEAT assuming no ICF correction and that determined by the ICF scheme of Delgado-Inglada et al. (2014) using only the Ar^{++} ionic abundance. High- and low-extinction PNe are marked separately. The dotted line shows the 1:1 line.

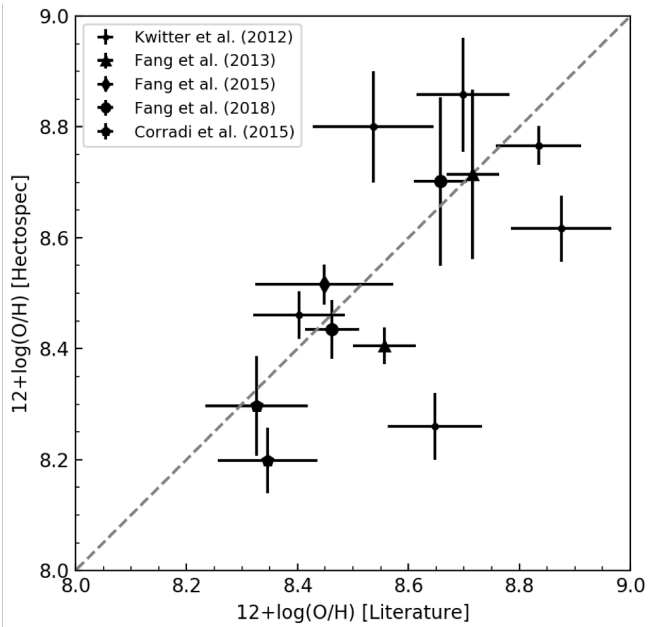

Figure B4. Comparison of the oxygen abundances derived in this work with those computed in the literature for the PNe in common. The PNe studied by different authors are marked with different symbols. The dotted line shows the 1:1 line.

ICF correction for unobserved O^{+3} ions can in theory be as high as ~ 10 times of the observed ions but this case happens when the PN central stars have high effective temperatures, T_{eff} ~ 200000 K (Delgado-Inglada et al. 2014, see their Figure 5). Given that such high ICF corrections is not the case for the PNe in this work where He I and He II recombination lines were observed, it is also unlikely that such high temperature central stars are present in the PNe where such lines are not detected. Thus, in this work we use the default NEAT prescription where the oxygen abundance is determined with ICF correction when He^{+} and He^{++} ionic abundances are measured and no ICF correction otherwise. We also note that ICF schemes from Delgado-Inglada et al. (2014) and Kingsburgh & Barlow (1994) give similar negligible corrections for oxygen abundance determination (García-Rojas et al. 2016; Fang et al. 2018).

Ionic abundances of Ar^{++}, Ar^{+3} and Ar^{+4} are estimated from observed [Ar III] 7136/7751 Å, [Ar IV] 4711/4740 Å and [Ar V] 7005 Å line fluxes respectively. While the [Ar III] 7136 Å line is observed for all 200 PNe where argon abundance is determined in this work, the other lines are observed for only a sub-sample of our PNe. The ICF scheme of Delgado-Inglada et al. (2014) is used for determining the argon abundance when only Ar^{++} ionic abundance is measured. However, as this ICF scheme does not incorporate Ar^{+3} and Ar^{+4} ionic abundances, the default prescription from NEAT does not carry out an ICF correction for argon abundance determination when multiple ionic species have their abundances determined. In Figure B3, we show that for the sub-sample of PNe where multiple argon ionic species are observed, the argon abundance determined by NEAT is consistent with that determined by applying the ICF scheme of Delgado-Inglada et al. (2014) to only the Ar^{++} ionic abundance. This is true for both high- and low-extinction PNe. Thus, whether only the [Ar III] 7136 Å line flux is measured or other forbidden argon lines fluxes are measured, we consistently determine the argon abundance in this work. We also note that ICF schemes from Delgado-Inglada et al. (2014) and Kingsburgh & Barlow (1994) give similar corrections for argon abundance determination (García-Rojas et al. 2016; Fang et al. 2018).

B4 Comparison of oxygen abundance estimates from this work with literature values

Figure B4 compares the oxygen abundances derived for PNe observed in this work which have oxygen abundances already published in the literature (Kwitter et al. 2012; Corradi et al. 2015; Fang et al. 2013, 2015, 2018). While most of the oxygen abundances values agree with each other, some scatter is observed. The scatter is particularly for the oxygen abundances determined in PNe by Kwitter et al. (2012) who employed 1D-CLOUDY (Ferland et al. 1998) photoionisation

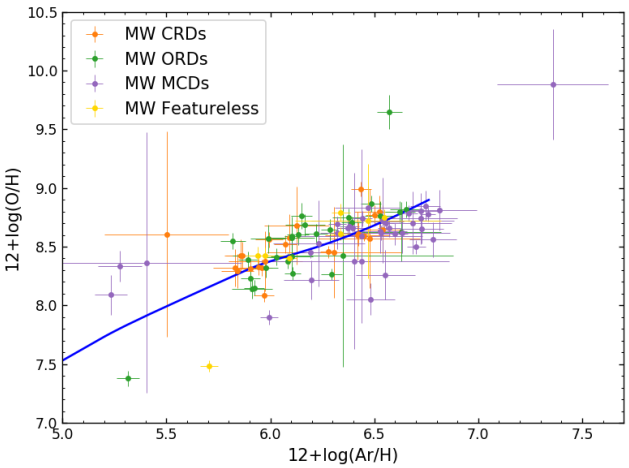

Figure C1. Oxygen vs. argon abundance distribution of 101 MW PNe marked by their circumstellar dust types from Ventura et al. (2017). The chemical evolution model track for the solar neighbourhood is from Kobayashi et al. (2020).

models to determine chemical abundances without relying on line-ratios. Note that the previously largest sample of PN abundances in M 31 (~50 PNe) were computed by Sanders et al. (2012) but since those have been reanalysed in this work, we do not show their previous estimates in Figure B4.

APPENDIX C: AGB EVOLUTION AND POSSIBLE DEPENDENCIES OF PN OXYGEN ABUNDANCES

While the derived argon abundances in PNe have been found to be invariant during the AGB evolution, thus reflecting the ISM abundance at the time of their birth, AGB evolution effects have been suggested to modify the oxygen abundance estimated in the nebula from that of the progenitor star, for specific PNe (Delgado-Inglada et al. 2015; García-Hernández et al. 2016). These effects depend on the progenitor mass and metallicity according to AGB theoretical evolution models such as those described in Ventura et al. (2017).

For PNe evolving from stars with initial mass $\geq 3M_{\odot}$, hot-bottom burning (HBB) may result in an oxygen depletion of up to ~ 0.2 dex, while for PNe evolving from stars with initial masses of $1-2M_{\odot}$ and Z< 0.008, third dredge-up (TDU) effects may result in an oxygen enrichment of up to ~ 0.3 dex (e.g. García-Hernández et al. 2016; Ventura et al. 2017). In a small sample of 20 MW PNe, Delgado-Inglada et al. (2015) found that oxygen is enriched in MW PNe with Carbon-rich (circumstellar) dust (CRDs), by up to ~ 0.3 dex for intermediate metallicities of 12+(O/H) = 8.2–8.7, while oxygen is invariant in MW PNe with oxygen-rich (circumstellar) dust (ORDs).

We therefore check whether the oxygen abundance values of a larger sample of MW PNe depend on the PN circumstellar dust composition. Figure C1 shows the distribution of oxygen abundances against the argon abundances of 101 MW PNe whose dust properties and abundances were tabulated by Ventura et al. (2017, their Sample 2). CRDs, ORDs as well as those PNe with featureless dust distribute around the ISM model predictions tracks for the solar neighbourhood (see Kobayashi et al. 2020 for details of the models). In particular, we compare the oxygen abundance of the PNe with that of the solar neighbourhood model at their given argon abundance. We find the MW CRDs and ORDs have mean offset in oxygen abundance of 0.06 dex ($\sigma_{\rm offset}$ = 0.26 dex) and 0.05 dex ($\sigma_{\rm offset}$ = 0.41 dex) respectively against the model. The featureless dust MW PNe have a mean offset of -0.02 dex ($\sigma_{\rm offset}$ = 0.43 dex) against the model. The offsets are much lower than the mean uncertainty, which is ~0.19 dex. The errors on the computed oxygen and argon abundances of the M 31 disc PNe in the current work are comparable to those of the MW PNe sample compiled by Ventura et al. (2017), as well as by Delgado-Inglada et al. (2015) for their statistically limited sample. We conclude that there is no segregation of CRD/ORD (as well as featureless) MW PNe in Figure C1.

We note also in the same figure that many of the MW PNe with mixed chemistry dust (MCDs) that are metal-rich (12 + log(Ar/H) > 6.3) preferentially have log(O/Ar) values below the model tracks, indicating lower oxygen or oxygen depletion. These MCDs have a mean offset of -0.13 dex ($\sigma_{\rm offset}$ = 0.21 dex) against the model. These PNe have been suggested by García-Hernández & Górny (2014) to be the youngest (<300 Myr), most metal-rich PNe in the MW sample. These PNe likely evolve from the most massive progenitors that display HBB, as predicted by the AGB evolution models discussed in Ventura et al. (2017). Thus, the log(O/Ar) values of MW PNe younger than ~300 Myr may be reduced due to oxygen depletion (see Figure C1). The M 31 low- and high- extinction PNe have average ages ~ 4.5 Gyr and ~ 2.5 Gyr respectively with the bulk of the latter having likely formed in a burst of star formation ~2 Gyr ago (Paper II). This implies that a very small number of PNe with very young massive progenitors (affected by HBB) are expected in our sample.

To summarise, we find no conclusive evidence of AGB evolution effects with modification of the oxygen abundance in the M 31 disc PNe studied in this work. Any such effect is within the measurement errors. We thus conclude the oxygen abundances derived for M 31 PNe reflect their birth ISM chemical abundances, within the errors.

This paper has been typeset from a TEX/LATEX file prepared by the author.